

Performance of wafer-fused VECSEL under high power operation

Stefan Keller

Master project, Departement Physik, ETH Zürich

*Dr. Vladimir Iakovlev**,

*Dr. Alexei Sirbu**,

*Prof. Dr. Eli Kapon**,

Prof. Dr. Jérôme Faist⁺

*EPF Lausanne, ⁺ETH Zürich

February 20, 2015

Abstract

I report on the performance of 1300 nm waveband wafer-fused vertical-external-cavity surface-emitting laser (VECSEL) in a thin disk (flip-chip) heat dissipation scheme. I investigate on its scaling behavior concerning output power and thermal resistance. The latter is assessed on whether it provides a useful tool for device metrology. An optimization strategy concerning one of the manufacturing steps is evaluated, and resulted in the record performance of 8.5 W output power with a conversion efficiency of 60 % at 5 °C heat sink temperature. The reflectivity off our device is found to change with heat sink temperature and pump power. Last but not least, the investigated wafer-fused samples did not show signs of degradation despite exposure of inhospitable measurement conditions.

Contents

| | | |
|----------|---|-----------|
| 1 | Introduction | 3 |
| 2 | VECSEL basics | 4 |
| 2.1 | Structure and design choices | 4 |
| 2.2 | Wafer-fusion | 6 |
| 3 | Thermal resistance | 6 |
| 3.1 | By spectral shift | 7 |
| 3.2 | By roll over | 8 |
| 3.3 | Remarks on experimental access and corrections | 8 |
| 3.4 | Power-scalability | 9 |
| 4 | Surface temperature raise, numerically | 9 |
| 4.1 | Pump beam profile | 10 |
| 4.2 | Pump profile dependent temperature increase on gain surface | 11 |
| 5 | Experimental Setup | 12 |
| 5.1 | Setup and sample | 13 |
| 5.2 | Measurement routine and error bars | 16 |

| | |
|--|-----------|
| 6 Results and Discussion | 18 |
| 6.1 Pump spot scalability | 18 |
| 6.1.1 Output power | 20 |
| 6.1.2 Thermal resistance | 22 |
| 6.2 Optimized emission output | 23 |
| 6.2.1 AR coating | 23 |
| 6.2.2 Reflecting metalization layer: record output | 26 |
| 6.3 Intrinsic roll over temperature | 28 |
| 6.4 Pump-induced change in reflectivity | 29 |
| 6.4.1 Observation | 29 |
| 6.4.2 Base reflectivity | 31 |
| 6.4.3 Explanation candidates | 32 |
| 7 Conclusion | 34 |
| A Alignment process, description of | 36 |
| B Spatial filtering | 37 |
| C COMSOL implementation | 39 |
| C.1 Heat source Q | 39 |
| C.2 Implementation of our VECSEL structure | 41 |
| C.3 Numeric convergence based on dimensionality | 41 |
| C.4 Explicit listing of simulation parameters | 42 |

1 Introduction

A vertical-external-cavity surface-emitting laser (VECSEL) is a special type of semiconductor laser. It converts low cost diode pump light into high beam quality laser emission. VECSELs combine the benefits known from solid state lasers, such as high output power with high beam quality, with the flexibility of semiconductor lasers and their coverage of bandgap engineered emission wavelength [1, 2, 3, 4].

The advantages of this technology made it attractive for a wide variety of applications, such as optical communication, spectroscopy, medical applications (both on detection and surgical side). VECSELs achieve high intra-cavity power which is ideal for non-linear optics. They can thus also be used to reach visible light via higher harmonics, which itself opens the field for laser TV and projectors. And frequency mixing also enables VECSELs to operate within the domains of microwave photonics, LIDAR, and THz sources [2, 5, 6, 7, 8, 9].

The 1300 nm waveband to date lacks options for high power laser sources. This range is particularly interesting [2, 6] to pump and laser process materials beyond the reach of conventional sub-micron light sources. Furthermore, the frequency doubled 650 nm red light fills an important gap for laser projection and spectroscopy. Additionally, this wavelength range benefits from pre-existing infrastructure and material development as a result of heavy investments of ICT.

Our VECSEL device is composed of a gain region grown by metallorganic vapor phase epitaxy (MOVPE) on a InP substrate incorporating AlGaInAs quantum wells. The distributed Bragg reflector (DBR) was grown by molecular beam epitaxy (MBE). These two elements were wafer-fused and Au-Au-bonded onto chemical vapor deposited (CVD) diamond, which itself was attached onto a water-cooled heat sink. I present more on VECSEL basics and about the wafer fusion in the following section. The gold bonding interface introduces beneficial thermal and optical properties; this will play a role as we try to improve the performance of our device. The manufacturing details are beyond the scope of this project, they can be found in [2, 10].

Numerical tools can be used to predict some of the VECSEL behaviors. Their usage, however, is fairly limited. This scarcity originates from the fact that in a VECSEL there are many effects to be considered: attempts have been made to calculate the absorption and gain of the quantum wells using semiconductor Block equations, considering spontaneous emission using semiconductor luminescence equations, and taking into account carrier losses using quantum Boltzmann scattering equations [11]. All of these steps rely on exact material parameters for a broad range of doping concentrations, operation temperatures, and wavelengths. The dimensionalities of a VECSEL chip along the plane and growth axes are different by orders of magnitude. This complicates the meshing procedure for finite element analyses, which is a problem the thermal simulations in particular suffer from.

On top of that, the optical pump conditions are usually ignored in numerical models. The pump spot profile is considered to be one of two simplest options to implement: a Gaussian or a flat-top profile; under normal incidence [2, 3, 11, 12]. Meanwhile, a more realistic pump profile would resemble something in between these two extreme forms, since the pump is usually delivered via a multi-mode fiber, under non-normal incidence [1, 4, 13].

As such, the simulations provide valuable insights in general trends of VECSEL behavior depending on particular parameters [11, 14]. But one should be very careful using the numerical results as a fit onto experimental results.

The goal of this project was to investigate – experimentally – the performance of our VECSEL structure under high power operation. This builds on previously published

work [2, 6]. Our idea is to learn about the power-scalability of our device, as well as to assess certain metrology processes. Based on the gained insights we then implemented two proposed strategies [11] to further improve the performance. The benchmark was set by the current record output power for the 1300 nm waveband of 7.1 W for a 300 μm pump spot diameter [6].

This report starts by discussing the concept of VECSELS from a general point of view. In section 2, I look at the basic elements involved in order to obtain an operating VECSEL device. Since VECSELS are rich in details, I have to restrain the introduction to the aspect of thermal management. The way heat flows throughout the structure is vital for its operation. In section 3, I introduce the concept of thermal resistance; a parameter that helps us to understand the heat extraction. This includes our understanding of this quantity from an experimental and numerical – in section 4 – point of view.

Given this general understanding of the important quantities, in section 5 I present our specific experimental setup and measurement routine aimed to extract said parameters. This leads to a discussion and interpretation of the obtained measurement results in section 6. I close this report with a summary and conclusion; and an outlook on how to advance the project given the current state of the VECSEL characterization. The appendices provide additional insights for some of the discussed points – but that do not belong to the core report.

2 VECSEL basics

In this section I introduce the concepts relevant to understand the presented measurements. The topic of VECSEL is rich and diverse: for more extensive reviews I direct to Tropper et al. [1] and Calvez et al. [5].

2.1 Structure and design choices

VECSEL stands for vertical-external-cavity surface-emitting laser. They are composed of three main sections: the confinement window, the gain region, and the active mirror. This mirror, together with an external output coupling mirror, form the laser cavity; thus the name. VECSELS are usually optically pumped. One of the characteristics of VECSELS is their ability to convert low quality pump to high quality emission light. The incidence angle is chosen to be convenient for the setup at hand [1], but should not be too flat, in order to limit the pump spot to elongate. Figure 2.1 illustrates the basic elements.

The active mirror is composed of a periodic structure of quarter wavelength semiconductor layers; a distributed Bragg reflector (DBR). The materials used for the DBR have to fulfill three basic requirements [5]. First of all, the material has to be transparent, i.e. non-absorbent, at the emission wavelength. Secondly, the used materials have to have a high contrast of refractive index. This helps to obtain high reflectivity with a low number of layers; smaller devices have advantageous thermal properties. Thirdly, the material used has to be as thermally conductive as possible.

The gain region is composed of quantum wells (QWs). They are placed at the antinodes of the standing-wave of the optical field of the design wavelength. This so-called resonant periodic gain (RPG) configuration helps to avoid spatial hole burning [2]. Figure 2.2 illustrates our VECSEL chip.

The confinement window (also known as cap) is transparent for pump and signal. Its function is twofold [1, 5]. First, it is designed to provide good coupling between the external and the sub-cavity. Secondly, it is a spacer to separate the surface from the carriers generated in the active region. This reduces non-radiative recombinations.

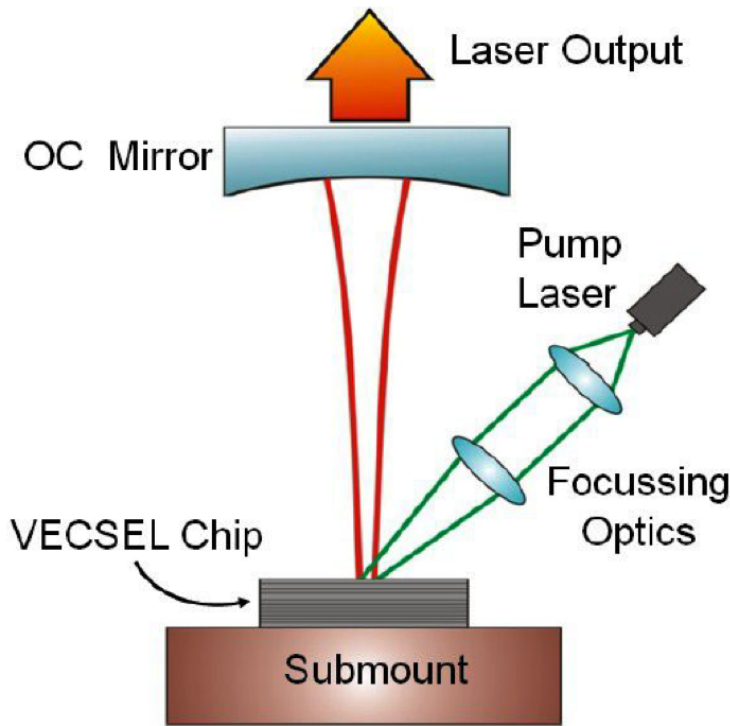


Figure 2.1: An optically pumped vertical-external-cavity surface-emitting laser (VECSEL) is composed of an output coupler external mirror (OC) and the VECSEL chip itself. The VECSEL chip is composed of a window layer (also known as cap), a gain region, and a mirror. It is mounted on a heat sink, and pumped by a diode laser. From [10].

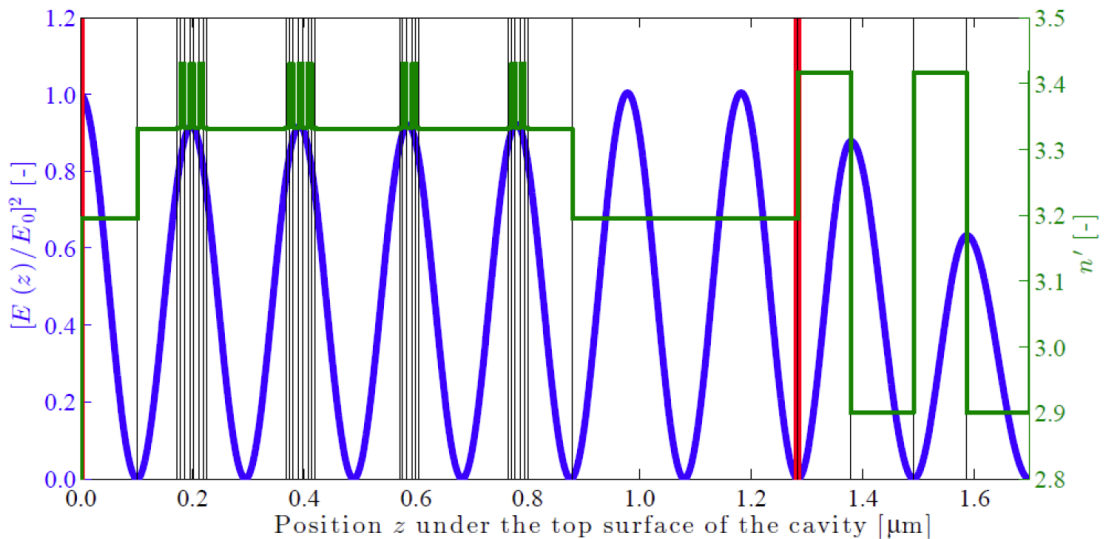


Figure 2.2: Schematic depiction of our VECSEL structure, from [10]. The first layer from left is the confinement window (also known as cap). It is followed by the gain region, up to the red line. This line indicates the wafer-fusion interface, after which follows the DBR. Only the first two layer pairs of the DBR are shown; there are 24 over all.

The thermal management is critical for the operation of VECSELs. Over the years, two strategies for heat extraction have been established [3, 14]: the heat-spreader, and the thin-disk approach. In the first strategy the VECSEL chip is grown in the order DBR–gain–cap, and the heat is extracted through a chemical vapor deposited (CVD) diamond clamped onto the cap. In the second approach, the structure is grown in reverse order, so the Bragg mirror can be bonded onto a CVD diamond. In this strategy the heat has to be extracted through the whole structure.

The heat-spreader approach tends to be more efficient to extract the heat – at least for relatively small pump spot sizes [14]. On the down side, it introduces Fabry-Perot effects, and makes the device packaging more bulky over all. For these reasons the thin disk approach would be preferred for a wide variety of applications [2].

2.2 Wafer-fusion

With our VECSEL design we aim to cover the $1.3\text{ }\mu\text{m}$ wavelength band. The corresponding material system for the active region is InP. DBRs grown on this material system do not provide high contrast in refractive index and have very low thermal conductivity. Because of the low contrast, more layers are required in order to obtain high reflectivity. And this is unfortunate for the thermal management, further aggravated by the low conductivity. Consequentially, the highest output powers in this waveband were obtained for wafer-fused devices [2]. For wafer fusion the active region is grown separately from the DBR and in a second step fused along the interface indicated in Fig. 2.2 with red line.

This approach corresponds to the thin disk strategy mentioned above. But it has the additional advantage to combine material systems whose design wavelength is around $1.3\text{ }\mu\text{m}$, with GaAs-based DBR, whose contrast in refractive index and thermal conductivity allows a more efficient heat extraction. This property is key for the high power performance of wafer-fused devices. Figure 2.3 shows a schematic illustration of our wafer-fused design. The DBR is bonded onto the CVD diamond using a gold interface. The DBR-Au bond itself is realized by employing titanium as adhesion layer.

Alternatives for the Au-Au-bonding involve intermediate In solder. But this material choice is disadvantageous for high temperatures [2]. Beside the structural necessities to use the gold layer, it is also predicted to show benefits for the thermal behavior and conversion efficiency of a VECSEL [11, 15].

The design and manufacturing process of the samples was not within the scope of this project. I thus constrain myself to explain only the essentials of these processes necessary to understand the report at hand. A more detailed description of the manufacturing process is given in [2, 10].

3 Thermal resistance

The thermal resistance (R_{th}) is the only experimentally accessible quantity to asses the heat flow in the structure [16]. The thermal management of a VECSEL is of critical importance [1, 3, 14, 17]. Consequentially, we're interested to determine R_{th} . It is a useful figure of merit to keep track of improvements on design and manufacturing process of VECSEL technology. The thermal resistance describes how much the sample heats up ($\text{d}T$) as a result of the dissipated power $\text{d}D$

$$\text{d}T = R_{\text{th}} \text{d}D \quad \Rightarrow \quad R_{\text{th}} = \frac{\partial T}{\partial D}. \quad (3.1)$$

There are several methods deployed to determine the thermal resistance, an overview can be found in [16]. Most of them are time and equipment intensive. This is impractical

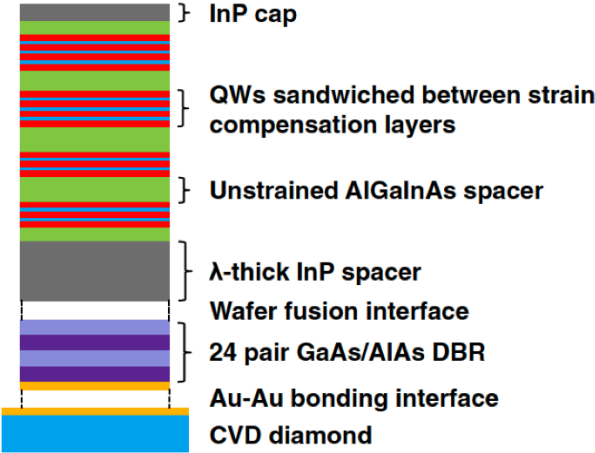


Figure 2.3: Our InP-based VECSEL design incorporating AlGaInAs quantum wells (QWs), wafer-fused, and bonded on CVD diamond. The λ -thick InP spacer acts as a defect blocking layer. The gain region was grown by metallorganic vapor phase epitaxy (MOVPE), the DBR was grown by molecular beam epitaxy (MBE). From [2, 10].

in order to monitor improvements made in a design and manufacturing process. More simple approaches are desired. For this report I review two methods that are supposed to be just that.

3.1 By spectral shift

We can write the thermal resistance from (3.1) as [16, 17]

$$R_{\text{th}} = \frac{\partial T}{\partial D} = \frac{\partial \lambda}{\partial D} / \frac{\partial \lambda}{\partial T}. \quad (3.2)$$

In this description λ corresponds to the longest emitted wavelength. The longest emitted wavelength is said to correspond to the hottest part of the VECSEL. This is a result of the predominantly linear shift in refractive index as function of temperature [16]. This approach ignores the change in cavity length resulting from thermal expansion.

The longest emitted wavelength is correlated with dissipated power. This gives a linear relation for each heat sink temperature

$$\lambda_{T_{\text{hs}}} = \left. \frac{\partial \lambda}{\partial D} \right|_{T_{\text{hs}}} D + \lambda_{0,T_{\text{hs}}}. \quad (3.3)$$

By substituting

$$\lambda_{0,T_{\text{hs}}} = \left. \frac{\partial \lambda}{\partial T} \right|_{T_{\text{hs}}} T_{\text{hs}} + \lambda_0 \quad (3.4)$$

we end up with [16]

$$\lambda = \left. \frac{\partial \lambda}{\partial D} \right|_{T_{\text{hs}}} D + \left. \frac{\partial \lambda}{\partial T} \right|_{T_{\text{hs}}} T_{\text{hs}} + \lambda_0, \quad (3.5)$$

from where we can extract the required parameters for (3.2) using linear regression.

We record the emitted spectrum for every pump setting. In order to determine the longest emitted wavelength we cut these spectra as indicated in Fig. 3.1. By measuring each pump setting multiple times, we can increase our confidence in the extracted wavelength value.

The dissipated power D corresponds to the left-over power of the pump (P), after we have accounted for the reflected (R) and emitted (E) part [16],

$$D = P - R - E. \quad (3.6)$$

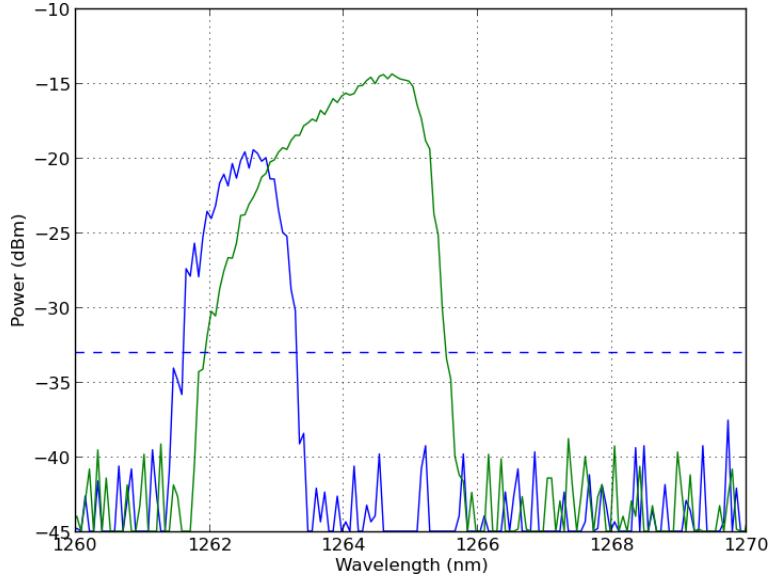


Figure 3.1: We cut the spectrum at a level above the noise floor. For each pump setting we have multiple measurements, giving us a margin of how reliable this extracted longest wavelength is.

3.2 By roll over

A second method, relies on an intrinsic roll over temperature. Roll over is an effect due to the optical pumping: While increasing the pump power in order to obtain higher emitted output, we heat the gain structure. This increase in temperature introduces an additional loss which the gain has to compensate. Otherwise, our device stops lasing. After a certain point the gain cannot compensate for the losses anymore, and this region stops contributing to the output. We see a decline in output power despite the higher pump – a roll-over.

Heinen et al. [16] have found empirically – using the method described in 3.1 – the longest wavelength at this roll over point is the same wavelength, regardless of the heat sink temperature. They conclude, this wavelength to correspond to an of the structure intrinsic critical temperature – the roll over temperature. Given definition (3.1) we find the difference in temperature between (unknown) roll over and heat sink. It is the thermal resistance times the dissipated power,

$$T_{\text{ro}} - T_{\text{hs}} = R_{\text{th}} D_{\text{ro}}. \quad (3.7)$$

In other words, when we plot dissipated power at roll over (D_{ro}) versus the heat sink temperature for this measurement T_{hs} , we find a linear relation. Its slope corresponds to the thermal resistance, and the y -intersection to the roll over temperature [16]:

$$T_{\text{hs}} = -R_{\text{th}} D_{\text{ro}} + T_{\text{ro}}. \quad (3.8)$$

This relation is wavelength independent. Mode instabilities in pump and emission are expected to result in fluctuations in the emitted spectra. A spectrum independent method to determine R_{th} is thus supposed to yield a result with smaller uncertainty. The difficulties in this second method arise from identifying the exact point of roll over. Whether this identification is more or less error-prone is open for discussion. Furthermore, it is not yet clear whether all VECSEL designs show this intrinsic roll over behavior.

3.3 Remarks on experimental access and corrections

Hader et al. [18] have pointed out, the used definition of dissipated power (3.6) ignores a relevant loss channel. Namely, beside the reflected, emitted, and dissipated part there are

additional non-heating losses the incident pump converts into. These additional losses come from non-heating spontaneous emission and surface-scattering. Without these we overestimate R_{th} . The losses due to surface-scattering are particularly pronounced when using an output coupler with low out-coupling losses.

From a theoretical point of view the comments made by Hader et al. [18] may be relevant. However, for the experimental approach they're impractical as the invoked calibration is tedious. Especially, if the main objective in monitoring R_{th} is to obtain a figure of merit for the thermal management of the VECSEL structure. As a remedy, Hader et al. suggest using an output coupler with higher out-coupling losses. The scattering losses would be less pronounced. In this report, I ignore these additional effects and work with (3.6). Consequentially, the stated values for the determined R_{th} 's are likely to overestimate the true value.

3.4 Power-scalability

The gain section of a VECSEL is very thin compared to the dimensions of the optical pump spot. This gain region is heated due to the difference in photon energy of pump and output and due to non-radiative recombinations. In other words, heat is extracted over a short path with respect to the pump spot size, and the resulting heat flow is approximatively one dimensional. Lateral cooling is therefore not as relevant for the operation of such a device. One dimensional heat extraction means the device is power scalable: increasing the pumped area does not introduce significantly additional heating. The output power can be enhanced by enlarging the pumped area, so more of the gain material is stimulated into emission. This is the expected behavior of disk lasers. [1, 19, 20].

Several effects hinder the real device to live up to these expectations. Bedford et al. [9] report a limit to this scalability: there is a critical diameter above which amplified spontaneous emission (ASE) and lateral lasing become relevant. These effects introduce additional losses which inevitably limit the output scaling. The pump beam shape was found to limit the power scaling further [4]. Furthermore, larger beam spots risk to be more susceptible to surface impurities and non-radiative defects [21].

If the thermal resistance R_{th} were to power scale, its value would have to decrease at an inverse rate of the pumped area, w^{-2} . As discussed by Giet et al. [17], this is not the case. Instead, the decrease in R_{th} follows more closely the radius (diameter) of the pump spot than the area, w^{-1} . This behavior is apparent when we plot spot size versus thermal resistance in a log-log plot. The slope in such a plot is closer to -1 than to -2 .

For the sake of completeness, the thermal resistance can be fitted with the empirical formula [17]

$$R_{\text{th}}(w) = a_1 + \frac{a_2}{w} \left(1 - \frac{w}{a_3}\right)^{1.5}. \quad (3.9)$$

This formula was adopted form a fit originally developed for VCSELs [22]. In the original form the ratio within the brackets represented the ratio between an inner and outer diameter of the VCSEL. Working with VECSELs we lack such a definition. As such, it is not clear what parameters $a_{\{1,2,3\}}$ are supposed to tell us about the VECSEL under test. So far, this description is not yet widely used by the scientific community.

4 Surface temperature raise, numerically

The commercial software COMSOL allows us to perform thermal simulations with a finite-element approach. The heat equation to be solved reads as

$$0 = \nabla(k\nabla T) + Q. \quad (4.1)$$

It is k the thermal conductivity of the material ($[k] = \text{m}^{-1}$), and Q the heat source ($[Q] = \text{W/m}^3$); originating from the pump beam. With this equation we take into account only conduction and ignore convection. In anisotropic materials the thermal conductivity differs depending on the direction of conduction. For the simulation we assume radial symmetry, in order to bring the 3D problem down to 2D. This saves computation time.

In this section, I cover some numerical considerations regarding the pump induced temperature increase within the different layers of a VECSEL structure. The presented plots show the expected temperature profile along the most important interface: the top of the gain section [2].

I only describe the new considerations made in the course of this project. While in appendix C, I explain where the formulae come from that are widely used in literature [2, 3, 12, 14, 19]. This appendix also provides additional insights, necessary to properly implement our structure in COMSOL. I start by introducing a beam profile that was so far not considered in these investigations. Eventually, I present the calculated pump induced temperature increase along the surface of the gain layer of our VECSEL structure, considering different pump powers and pump beam profiles.

4.1 Pump beam profile

For the heat source Q in (4.1) we assume the pump beam is incident antiparallel to the z -axis (here referred to as from the top), and of Gaussian profile. In this orientation the heat source associated with each layer j of the structure is given as [3]

$$Q_j = \frac{2P}{\pi w^2} \eta_j \alpha_j e^{-\frac{-2r^2}{w^2}} e^{-\alpha_j(z_{0j}-z)} e^{-\sum_{i < j} \alpha_i t_i}. \quad (4.2)$$

This representation counts the layers from the top down – the sum $\sum_{i < j}$ includes the layers on top and ignores those below the layer of interest (in that case j). A derivation, as well as a more in-depth explanation what the different parameters stand for, is given in appendix C.1.

Equation (4.2) describes a Gaussian pump profile by design. In reality, however, the pump profile is most likely not Gaussian. In fact, the pump spot imaged from a multimode fiber resembles a flat-top (also known as top-hat) distribution [1], or at least a super-Gaussian [4, 13]. Figure 4.1 illustrates the difference in beam shape of these mentioned three types.

In order to incorporate a flat-top pump profile, we have to replace the Gaussian part in (4.2) [12]:

$$2e^{-\frac{-2r^2}{w^2}} \rightarrow \begin{cases} 1 & r \leq w \\ 0 & r > w. \end{cases} \quad (4.3)$$

This can easily be verified as the renormalization has to match,

$$\frac{2}{w^2} \int_0^\infty r dr e^{-\frac{-2r^2}{w^2}} = \frac{1}{w^2} \int_0^w r dr = \frac{1}{2}. \quad (4.4)$$

A super-Gaussian is of the form [4]

$$f(x) \propto e^{-|\frac{x}{w}|^\beta}. \quad (4.5)$$

The Gaussian profile (C.5) corresponds to the special case $\beta = 2$, and the flat-top distribution to $\beta = \infty$. Parameter w corresponds to the e^{-2} radius

$$w = \frac{\text{FWHM}}{2(\frac{1}{2} \log 2)^{1/\beta}}. \quad (4.6)$$

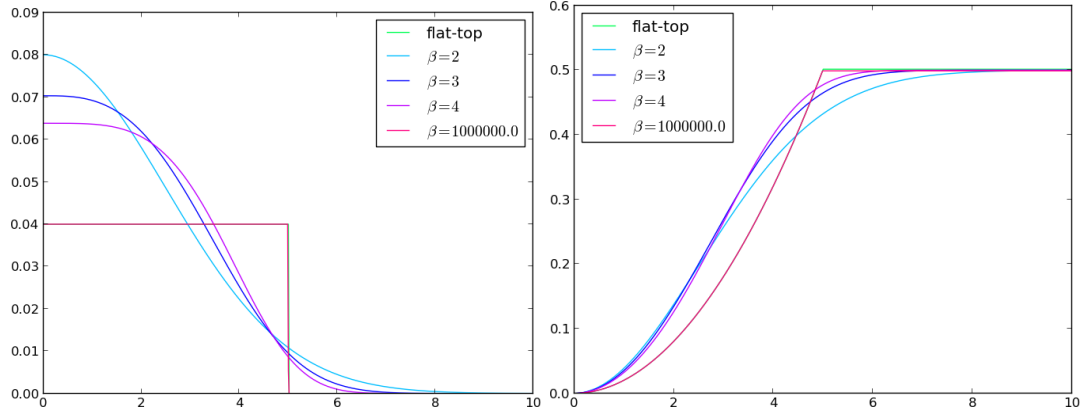


Figure 4.1: A super-Gaussian of the form $f^2(x) \propto e^{-2|x/w|^\beta}$ [4] describes an intermediate shape between a regular Gaussian with $\beta = 2$ and flat-top with $\beta = \infty$. Left, we see the squared shapes of super-Gaussians $f^2(x)$ with $w = 5$ for different values of β , including flat-top as a point of reference. The normalization is chosen such that the overall integral corresponds to 0.5; from (4.4). This is demonstrated in the plot to the right.

This definition of w is necessary in order to be compatible with the definition of the flat-top distribution already known in literature [12]. However, in [13] they measured the profile of their super-Gaussian pump, and decided to report the FWHM as spot diameter.

Before we can incorporate a super-Gaussian, we have to numerically find the normalization factor

$$a_p = \frac{2}{w^2} \int_0^\infty r dr e^{-2|\frac{r}{w}|^\beta}. \quad (4.7)$$

Analogously to (4.3), for a super-Gaussian profile we replace in (4.2)

$$2e^{-\frac{2r^2}{w^2}} \rightarrow \frac{1}{a_p} e^{-2|\frac{r}{w}|^\beta}. \quad (4.8)$$

Four examples for the normalization factor, rounded to four digits, are $a_2 = 0.5$, $a_3 = 0.5687$, $a_4 = 0.6267$, and $a_\infty = 0.5$. See also the analytic results in (4.4), and Fig. 4.1.

4.2 Pump profile dependent temperature increase on gain surface

With the concepts described in appendix C and section 4.1 we can look at the expected temperature increase of our structure, corresponding to different pump beam profiles. The thermal load inflicted on the structure depends on this pump distribution. The image of a multi-mode fiber can be described by a super-Gaussian. This category describes a generalized Gaussian profile of the form $f(x) \sim e^{-|\frac{x}{w}|^\beta}$ [4], see Fig. 4.1. It covers distributions between Gaussian ($\beta = 2$) and flat-top ($\beta = \infty$). The closer the pump beam distribution resembles a flat-top distribution, the more evenly the temperature load is distributed.

The numerical analysis for super-Gaussian profiles is particularly interesting: while the temperature profile caused by Gaussian and flat-top distributions were already reported [12], the intermediate super-Gaussian profile was ignored thus far. The fact that the pump profile is relevant for the performance of VECSELs was demonstrated in [4].

We can assume roll over occurs once the gain material exceeds a critical temperature [16], see section 3. In order to postpone the critical pump power to higher values, we have to lower the peak temperature invoked by the pump. Figure 4.2 shows, this can be

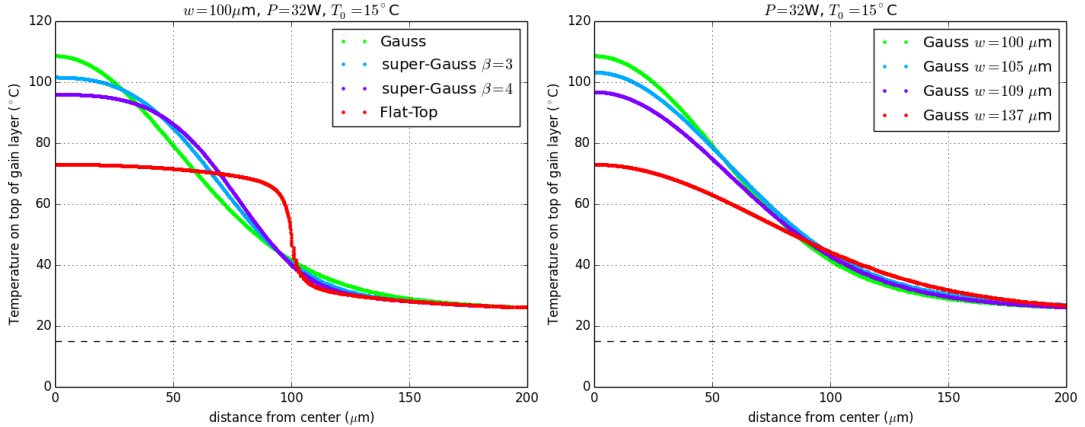


Figure 4.2: Temperature along surface of the gain section, z_{0g} (Tab. C.2). The different beam shapes from Fig. 4.1 with the same total power induce a different increase in temperature with respect to T_0 , indicated by the dashed line (left). The same peak temperature can be found employing regular Gaussians with larger beam spots. These however, have a larger fraction of the power distribution below threshold in the tail region, which contributes only to heating but no light emission.

achieved by either assuming a super-Gaussian beam profile or a regular Gaussian with larger spot size.

The peak temperature is not the only relevant quantity for an efficient pump profile: the gain needs to be irradiated with enough power to transcend threshold. The regions of the sample irradiated by pump light but below threshold do not contribute to the laser output. However, these regions do heat the structure.

The stronger we pump, the larger the area on the sample irradiated by above-threshold power. This above-threshold region corresponds to the relevant, effective area. In the case of the accentuated Gaussian beam, the center exceeds the roll over temperature at a relatively low pump power, while the effective area is still relatively small. In contrast, a super-Gaussian pump profile is capable activating a larger effective area, while at the same time lowering the peak temperature. Consequentially, roll over is expected to occur at higher pump power.

These simulations demonstrate the thermal management depends on the pump profile. Furthermore, they suggest a Gaussian pump profile to be non-ideal concerning the inflicted thermal load. This reasoning is consistent with the findings in [4].

This provokes me to issue a warning: extracting thermal resistance R_{th} only for the hottest spot, as suggested in section 3, does not tell the full story. We can find normal Gaussians with the same peak temperature as super-Gaussians, Fig. 4.3. Comparing thus extracted values of R_{th} with values measured with other setups – and expectedly different pump profiles – is hence not valid.

5 Experimental Setup

The main objective is to look at the high power regime, attractive for intra-cavity frequency mixing. For this, I report on the light-light performance of 1270 nm waveband VECSELS with wafer fused gain mirrors set in the flip-chip heat dissipation scheme, see section 2. The light-light characteristics relates the pumped input power with the converted emission power. is recorded for various heat sink temperatures. To asses the thermal management we determine the thermal resistance of our device. Following section 3, we have to keep track of the pumped, reflected, and emitted power, and the

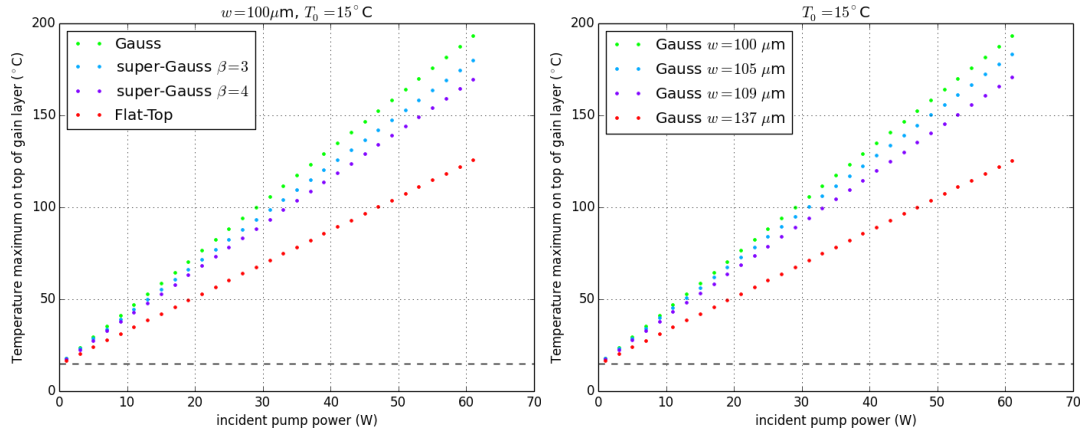


Figure 4.3: The maximum temperature (i.e. at $r = 0 \mu\text{m}$) of the different beam profile depicted in Fig. 4.2, for various settings of total power. The increase in peak temperature does not change qualitatively whether we consider super-Gaussians (left) or regular Gaussians with larger radii (right).

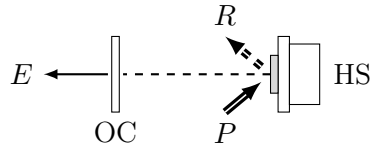


Figure 5.1: The sample is mounted on a water cooled heat sink (HS). The external cavity is defined by the output coupler (OC) and the active mirror attached to the HS. The pump is incident at approximately 36° , with power P . We are further interested in the emitted power E , and the reflected power R .

emitted spectra.

5.1 Setup and sample

Figure 5.1 depicts the basic scheme of the used setup: The VECSEL sample is mounted on a water cooled heat sink, and is optically pumped by power P , with a pump spot size of radius w . Some of this pump light is converted and emitted (E), reflected off the sample (R), and the rest is said to be dissipated (D), through the sample onto the heat sink. For the light-light characteristics we are interested in the relation between P and E . Respectively, we are interested in how much of the net pump light is converted into emitted light. This net pump we signify as absorbed power

$$A = P - R. \quad (5.1)$$

This definition of absorbed power overestimates the real absorbed power, it ignores surface scattering and spontaneous emission outside the cavity. For the experiments presented this report, I ignore these loss channels.

The pump is a 980 nm diode laser. Figure 5.2 illustrates the spectrum for two different pump currents. The pump is delivered by a multimode fiber. We image its end onto the sample, under an incidence angle of approximately 36° , using various lenses. This results in the various spot diameters $2w = \{180, 200, 300, 333, 400, 444\} \mu\text{m}$. To ensure good mode overlap the cavity lengths has to be adjusted.

The VECSEL-sample is designed to emit around 1270 nm. The fabrication details are published elsewhere [2, 10]; they are not part of this report. The essential details are

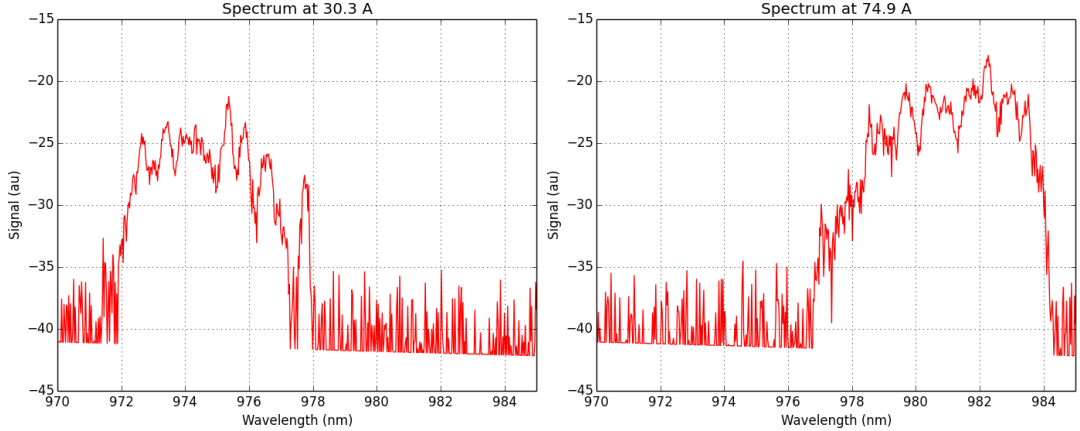


Figure 5.2: Spectrum of nominally 980 nm pump beam; measured at ≈ 6 cm distance to divergent pump delivery fiber, under 0° incidence. The plots correspond to an optical output of 21 W and 56 W, respectively.

highlighted in section 2, section 1.

Monitoring the reflection off the sample is crucial for high power operation. For one, we want to design the VECSEL structure such that it absorbs as much of the pump light as possible. Secondly, depending on the exact application the VECSEL is used for, the reflected light may pose a health hazard; or at least an additional heat spot that needs to be taken care of.

The thermal resistance R_{th} connects the sample temperature with the dissipated power (3.1)

$$T = R_{\text{th}}D. \quad (5.2)$$

The performance of a VECSEL depends on temperature. The thermal management of the device is thus critical [1, 3, 14] and thus a low thermal resistance is desired. Furthermore, the thermal resistance is the only experimentally accessible quantity to assess the heat flow in a VECSEL [16]. Beside the quantities mentioned in Fig. 5.1, in order to estimate the thermal resistance we also need to record the spectrum of the emitted light [2, 16], see section 3.

Figure 5.3 shows a photograph of our setup. It meets the specifications to measure pumped, reflected, and emitted power, as well as the spectra simultaneously. The pumped and reflected power we measure by sampling a fraction of the beam. The reflectivity of these beam sampler depend on the incidence angle. This beam sampling fraction needs thus to be recalibrated whenever we change the beam sampler configuration. We have to adjust the configuration for example when we change the pump spot size.

The pump spot size we vary by changing the lenses used to image the fiber end onto the sample. In Fig. 5.3 these are denoted as L_{p1} and L_{p2} . The distance between delivery fiber and the first lens has to correspond to its focal length. In this configuration the beam after the first lens is collimated. This arrangement we test by eye, with the help of an IR-viewer. The pump spot is at a distance of a focal length after the second lens.

In order to find the exact distance, we look for the alignment with the lowest lasing threshold – visualized by a camera in the emission path. This initial position is further optimized during the fine-alignment of the output coupler, aiming at optimal output power.

The ratio in focal lengths of the two employed lenses corresponds to obtained spot size. I report the usage of two types of lenses for lens L_{p1} : a plano-convex, spherical lens motivated by the publications by Heinen et al. [13, 16]; and a plano-convex, achromatic lens. Given the fairly narrow pump spectrum depicted in Fig. 5.2 we wouldn't expect the

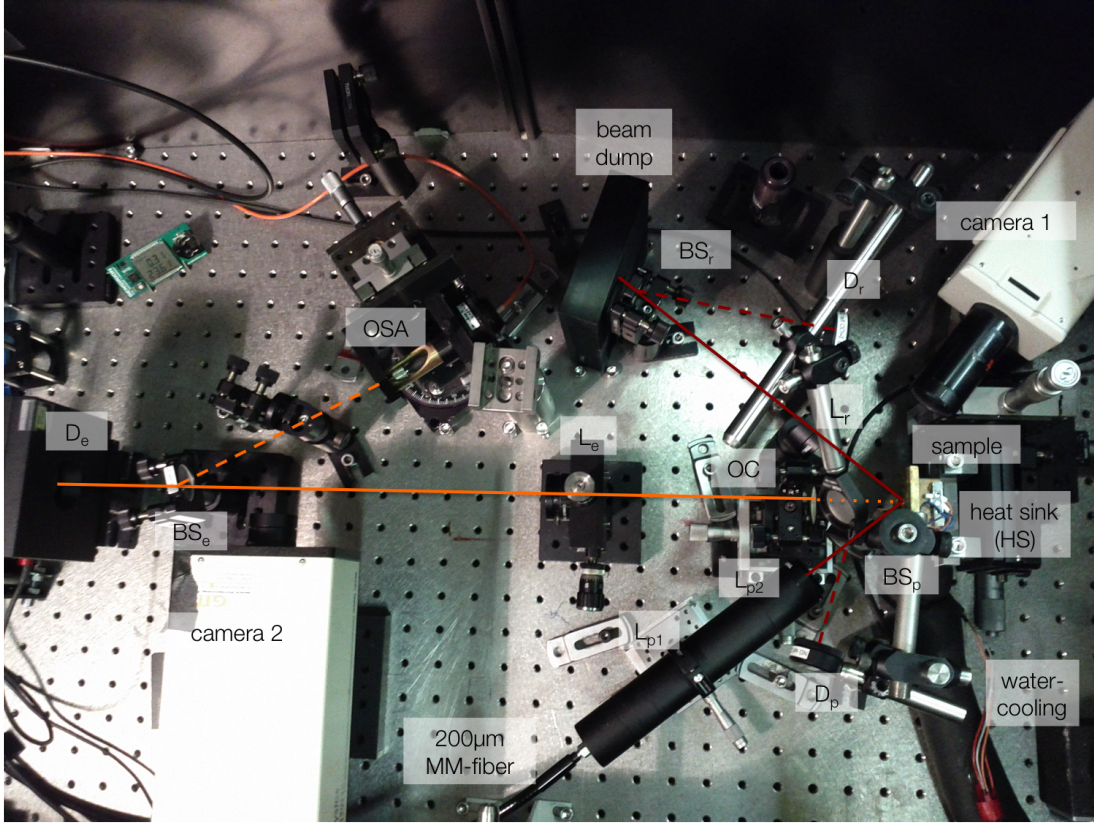


Figure 5.3: The pump light is delivered with a $200\mu\text{m}$ multimode (MM) fiber whose end is imaged onto the sample. The sample is mounted on a water cooled copper heat sink. We image using various lenses (L_{p1}, L_{p2}), resulting in various spot sizes. The reflected, divergent light is collected by lens L_r and subsequently directed onto a beam dump. The two beam sampler (BS_p and BS_r) probe a fraction of the pumped and reflected light. This beam sample is directed to their respective detectors (D_p and D_r). The sample, together with the output coupler (OC), form the external cavity. The OC has an output coupling loss $\alpha_{\text{OC}} = 2.5\%$, and a radius of curvature $ROC = 50\text{ mm}$. The VECSEL emission is collected by lens L_e and directed onto power meter D_e . A fraction of this output is extracted by beam sampler BS_e and directed onto the MM-fiber connected with the optical spectrum analyzer (OSA). The polarization of neither pump nor emission is filtered, in our setup we do not distinguish between polarization dependent phenomena. Cameras 1 and 2 facilitate the alignment.

achromaticity itself to have much of an effect. On the other hand, the achromatic doublet has been corrected for various aberrations [23]. This may contribute a relevant beam property. All lenses, as well as the beam samplers, are appropriately coated (meaning B- and C-coated in the pump and emission branch, respectively).

The sample is attached on a ceramic plate, which itself is attached to a water cooled copper block, using thermal grease. The reported heat sink temperature is the temperature we measure at the copper block. Due to the irradiated power the heat sink cannot keep a constant temperature. As a result the measurements see a fluctuation of about $\pm 1^\circ\text{C}$ standard deviation. These temperature fluctuations are addressed again in subsection 5.2.

I have worked with two samples, addressing a proposed optimization strategy [11]. A magnified photo of sample 1 is shown in Fig. 5.4. It is illuminated by 980 nm pump light, highlighting the defects that don't contribute to photo luminescence. The camera has burnt spots itself. In order not to confuse the camera defects with those of the structure, I have covered those of the camera with blue dots. The presented measurements were taken when irradiating either of the two regions denoted as A and B, respectively.

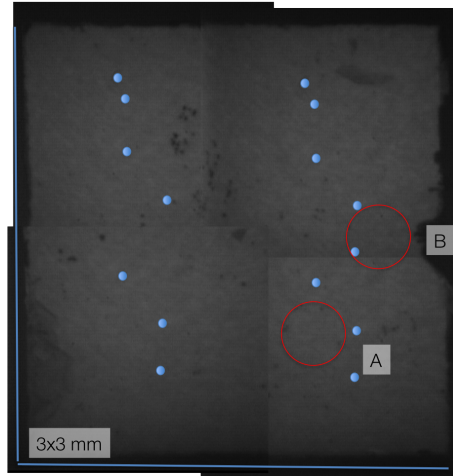


Figure 5.4: Sample 1. Used for pump spot scaling. Magnified by a microscope, illuminated with 980 nm light. This light source makes visible the defects of the structure; as the dark spots will also be dark when pumped during laser operation. The blue dots cover defects of the used camera, which otherwise may be mistaken as defects of the sample. The red circles indicate irradiation region A and B, respectively. The sample dimensions are 3×3 mm.

We investigate the effect of two optimization strategies [11]. First, we have coated this same sample 1 with an anti-reflection coating. The surface integrity after the necessary surface treatment and coating is shown in Fig. 5.5. It doesn't highlight the surface roughness which visibly worsened because of the coating. This lead to poorer performance, as will be discussed in section 6.2.

For the second optimization the gold layer between the DBR and the CVD diamond is treated to be highly reflective. For this measure we have to take a second sample. Its active region and DBR are identical with those of sample 1. Figure 5.6 shows the surface integrity of sample 2.

5.2 Measurement routine and error bars

For each light-light characteristic we vary the incident pump power P and the temperature of the heat sink T_{hs} . The varying heat sink temperature is required to determine the thermal resistance, see section 3.

The heat sink temperatures are partially set in ascending and descending order, Fig. 5.7. This allows us to save time, since the heat reservoir providing the temperature stabilized water is inert. On the other hand, this routine also indicates whether the results are consistent or depend on the temperature cycle they were measured in. And last but not least, this routine allows us to see whether or not the sample takes damage as a result of the elevated temperature; a property vital for real world applications.

At each heat sink temperature we irradiate the sample with different pump powers. Each pump is repeated N times over all. The pump order is selected at random, as illustrated in Fig. 5.8. Thanks to the random sampling the measurement results are detached from the lab environment – most notably time-independent. The heat sink cannot control its temperature with absolute precision. Figure 5.9 illustrates this issue: It shows the actually present heat sink temperature for six set temperatures. In the left column the temperatures are plotted in chronological order. We can identify, the temperature drifts. The right column shows the same temperatures, but corresponding to the set pump. The repeated measurements see a spread of different temperatures but the temporal drifts can not be resolved.

In contrast, Fig. 5.10 shows the heat sink temperature during a measurement without

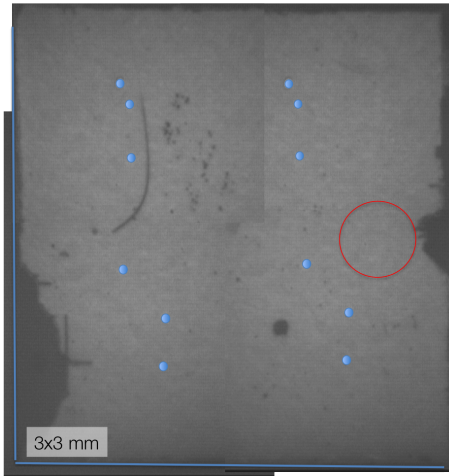


Figure 5.5: Sample 1 from Fig. 5.4, after surface treatment and AR coating. The brightness cannot be compared with the one from Fig. 5.4, the camera is not calibrated for such a comparison. The illumination at 980 nm shows non-radiative defects, but it doesn't show the surface roughness. The red circle indicates the tested spot.

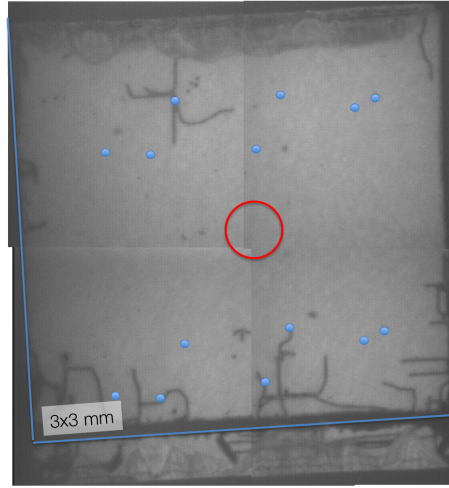


Figure 5.6: Sample 2. Used to investigate an optimization strategy: reflecting metalization layer behind the DBR. The brightness cannot be compared with the one from Fig. 5.4, the camera is not calibrated for such a comparison. The 980 nm light source makes visible the non radiative defects of the structure. The blue dots cover camera defects. The red circles indicates the tested spot. The sample dimensions are 3×3 mm.

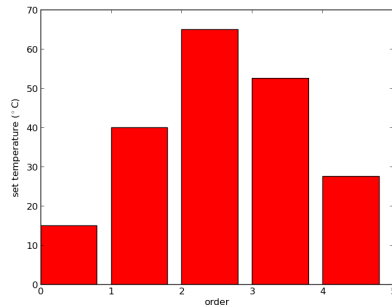


Figure 5.7: An example for the temperature order. Some of the temperatures are set while heating up, the rest while cooling down. The objective is to save time, to have a consistency check, and to see whether the sample shows fatigue after heating it up.

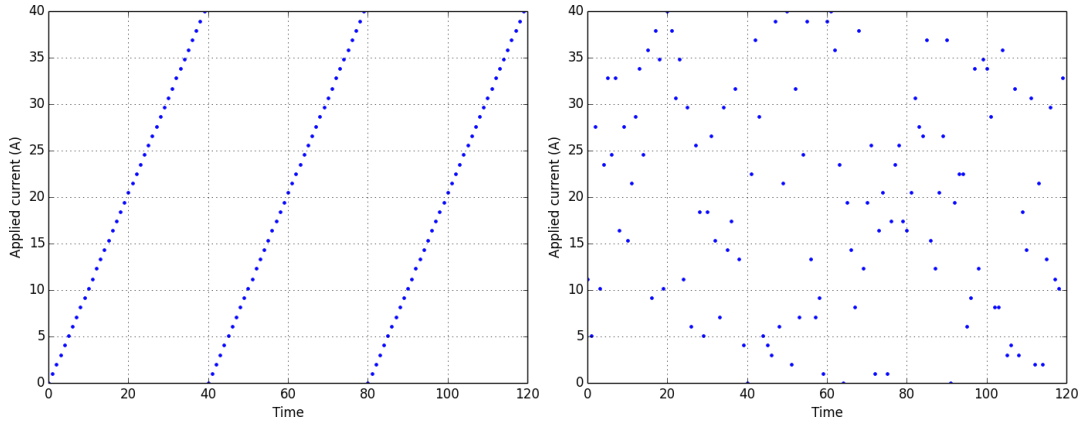


Figure 5.8: Two examples to apply various pump settings, with a repetition rate of 3. Left: A ramp. Right: Random sampling.

the random pump selection. In this case, clearly, we cannot talk about a single heat sink temperature for all the pump settings for this specific set heat sink temperature. The resulting measurements are highly repeatable, but only given the same pump order. This pseudo-stability we exploit during the calibration process of the different beam samplers and detectors: During the calibration we don't care about reproducibility but solely about the repeatability of two consecutive measurements.

The power meter average each measurement point over 200 samples, of which each one sample takes approx. 3 ms [24].

As mentioned already, we repeated the measurement of each pump setting N times. With this repetition we obtain a measure for how well we know the underlying true value. We are hence interested in the mean of these single measurements and the resulting unbiased standard error [25]

$$\Delta x = \sqrt{\frac{1}{N(N-1)} \sum_{i=1}^N (x_i - \bar{x})^2}, \quad (5.3)$$

For the uncertainties attached to quantities obtained through fits, I use a so-called Jackknife [26] approach: In a nutshell, this method allows to estimate the influence of the single measurement points on the fit parameters without working through the covariance matrix of the fit. The resulting error value is directly related with the unbiased standard error (5.3), used for the rest of the report.

6 Results and Discussion

In this section I discuss the power scaling of our device, the thus learned lessons in order to improve the performance, and an assessment of the usefulness of the thermal resistance as a figure of merit to evaluate the samples. I close this section with the presentation of an unexpected behavior of the reflectivity of our VECSEL device.

6.1 Pump spot scalability

One way to augment the output power is to increase the pumped area [1, 4, 21]. A power scalable device would increase the output power proportional to the irradiated area. As described in section 3.4, this ideal description doesn't work for real VECSELs; the lateral cooling is important after all [4].

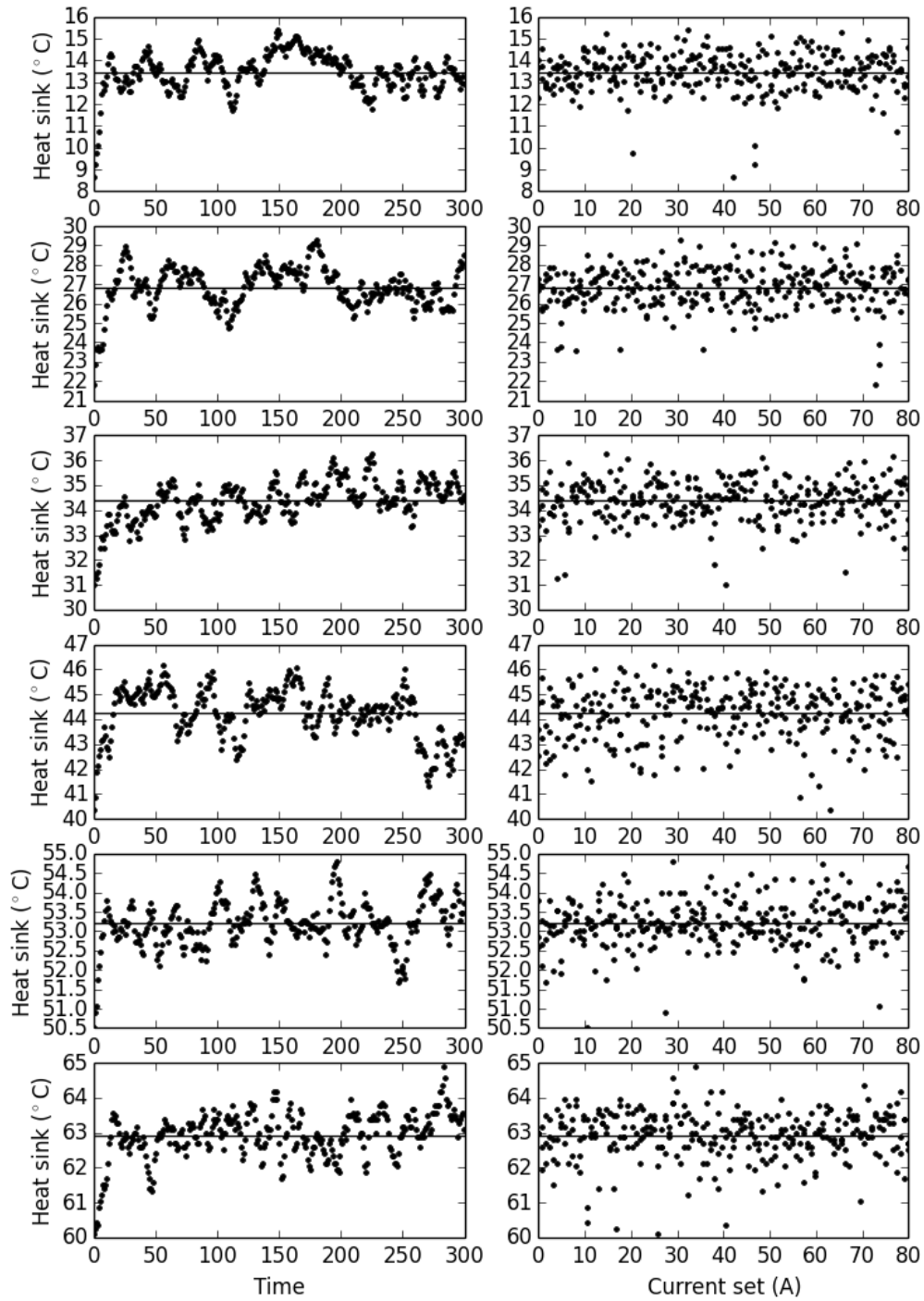


Figure 5.9: The heat sink temperature fluctuates over time (left). Thanks to the random sampling addressed in Fig. 5.8 the measurements don't see these drifts (right).

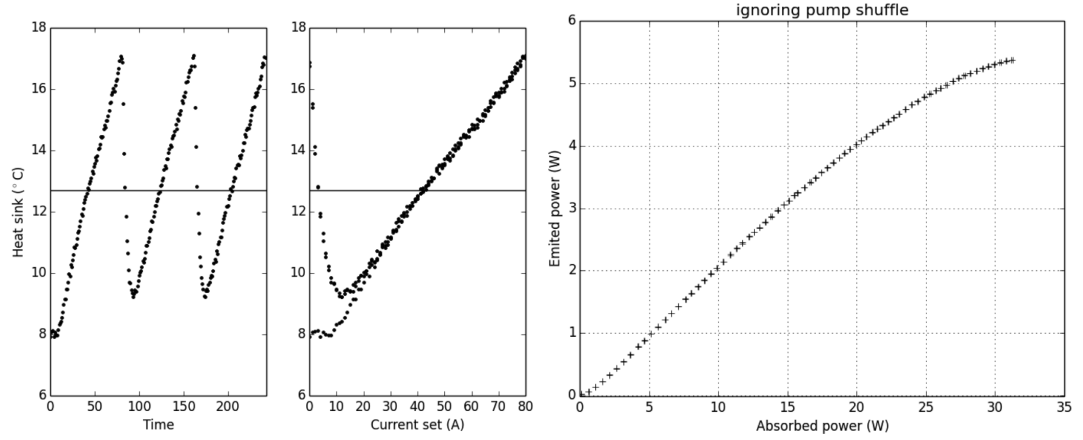


Figure 5.10: In contrast to Fig. 5.9, when we ignore the random pump sampling highlighted in Fig. 5.8, the temperature seen by the single pump settings differ strongly from the average heat sink temperature (left). The resulting LL-characteristic has very little noise on its data points (right). But these small error bars dismiss the fact that the underlying points were measured under very different conditions; eroding the significance of this low noise.

By investigating the scaling behavior we can learn about the limits of the performance of our device. We vary the pump spot size using lenses with various focal lengths in order to image the $200\text{ }\mu\text{m}$ diameter fiber onto sample 1, see section 5.1. For the scaling experiments I irradiated spot A indicated in Fig. 5.4. Because of the change of lens L_{p2} and the subsequent realignment of the setup, I cannot ensure to have hit the exact same spot. The employed cameras help us to find it approximately, but the remaining uncertainty is hard to estimate. I imply the sample is homogeneous enough on this scale. Each data point is measured $N = 3$ times.

6.1.1 Output power

In order to learn about the scaling behavior of the output power, we look at the light-light characteristics obtained from different pump spot sizes. Output scaling with area only works up to a point, above which amplified spontaneous emission (ASE) losses become significant [27]. Bedford et al. [9] also estimate there to be a critical diameter above which lateral lasing is likely to occur before the intended transversal lasing. With our measurements, we're interested to see the experimental scaling behavior of our structure for spot sizes realistic in real world applications.

Figure 6.1 plots the resulted light-light characteristics for various spot sizes, measured at the heat sink temperatures $\{15, 30, 45\}^{\circ}\text{C}$, using spherical lenses for both L_{p1} and L_{p2} . The average maintained heat sink temperature, plus-minus its standard deviation, is stated in each of the subplots, accompanied by the slope efficiency corresponding to the straight lines. The slope efficiency is obtained by taking into account only the data points of the linear segment. The onset of the roll over region is ignored.

The most obvious conclusion we can draw from these measurements is that our device is not power scalable: the conversion efficiency decreases for larger pump spots, while in a scalable device it should not. Consequentially, the maximally achieved output power is not increased for larger pump spots. In order to explain this we acknowledge that with larger pump spots we're more likely to hit non-radiative defects [21]. Secondly, the thermal resistance is empirically demonstrated to decrease less efficiently than with irradiated area. The initial explanation why VECSELs are expected to power scale relies on the one dimensional heat extraction. In reality the contribution of lateral cooling

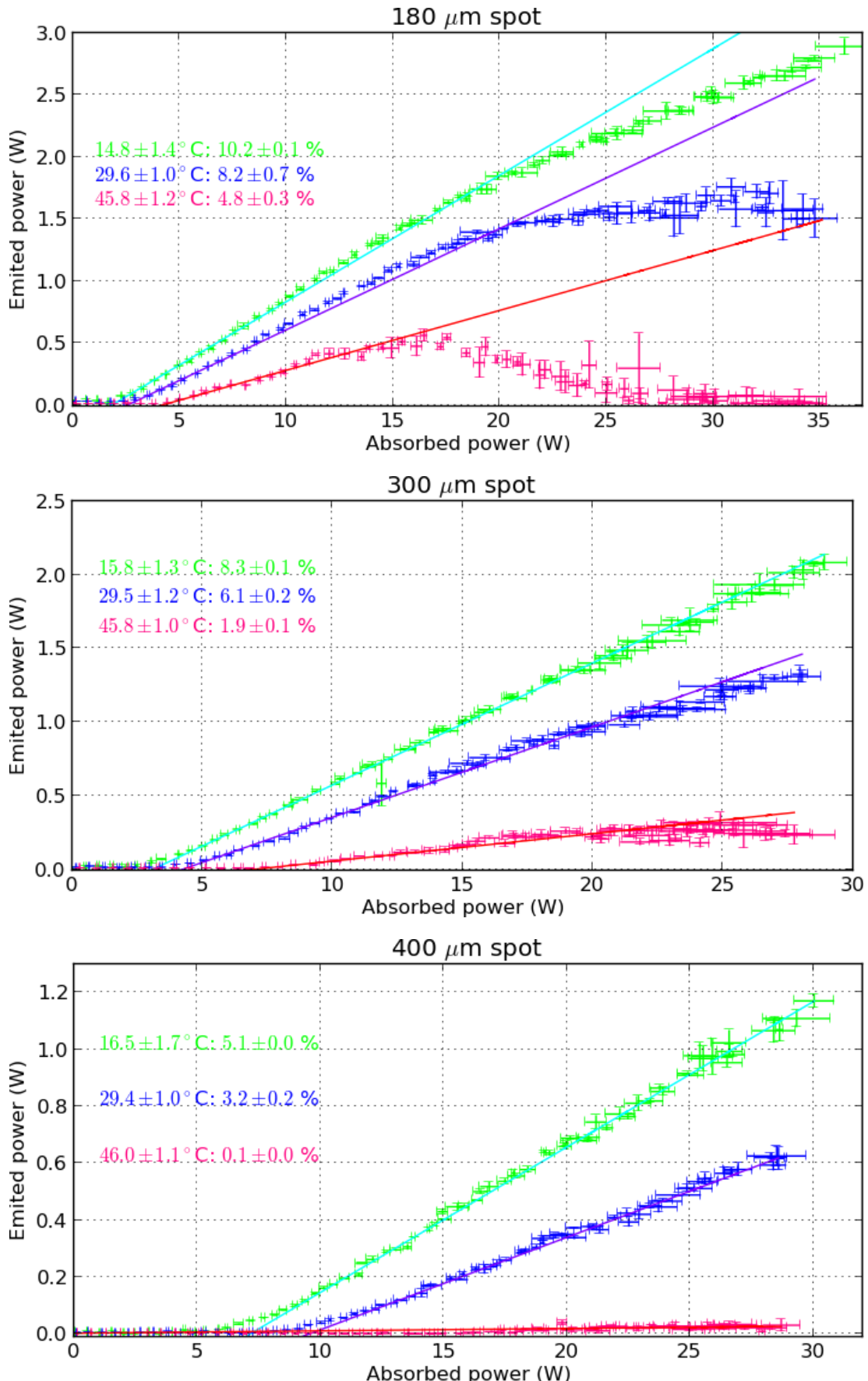


Figure 6.1: Light-light characteristics for different spot sizes obtained with spherical lenses. The efficiency decreases for increased spot size. This may be due to inefficient heat extraction manifested in sub-area scaling of R_{th} , discussed in section 6.1.2.

must not be neglected [28].

Beside the decrease in conversion efficiency, the roll over point shifts to higher absorbed power for larger pump spots. This indicates the structure to heat up less for larger pump spots. The findings concerning the thermal resistance discussed in 6.1.2 support this interpretation.

I performed these scaling measurements also with lens L_{p1} replaced by an achromatic lens. We would not assume to find significant differences in the scaling behavior since the spectral profile of our pump source is fairly narrow, Fig. 5.2. Nevertheless, this assumption needs to be tested. Secondly, these measurements yield additional data points for the thermal resistance scaling behavior, discussed in 6.1.2.

The investigated spot diameters are $\{222, 333, 444\} \mu\text{m}$ for the achromatic configuration. The used output coupler is not optimal for spot sizes larger than $400 \mu\text{m}$. The performance corresponding to the $444 \mu\text{m}$ spot was indeed worse than the one corresponding to the $333 \mu\text{m}$ spot. However, the $222 \mu\text{m}$ spot performed even worse. Given this discrepancy, I have to discard the results from the spot scaling experiments in the achromatic setting. Non the less, all of these three measurements showed an improved performance with respect to the spherical lens configuration.

We don't know the exact beam shape, and the estimation of the spot size is the result of a ray optical consideration. The uncertainty resulting from this approach should be looked into more closely in future investigations. The fact that the pump beam shape is relevant was demonstrated in [4]. The improved output performance seen in our setup, by simply changing the type of one of the pump delivery lenses, also indicate on the importance of the pump profile. A summary on beam shape alteration is given in appendix B and [29].

For now we can only speculate why incorporating the achromatic lens improves the output performance the way it did. I investigated the $333 \mu\text{m}$ configuration more thoroughly. The results were reproducible and thus credible. The measurements concerning the proposed improvements [11] presented in section 6.2, were obtained in this configuration.

6.1.2 Thermal resistance

In order to determine the thermal resistance R_{th} we have to look at the longest emitted wavelength λ at different heat sink temperature versus dissipated power D , (3.6). According to the method described in section 3.1 we can find a linear relation between λ and D , from which we can deduce the thermal resistance R_{th} . We do this for the different spot sizes, and can thus conclude on the scaling behavior.

The spot sizes $\{180, 300, 400\} \mu\text{m}$ were each measured for the temperatures $\{15, 30, 45\}^{\circ}\text{C}$, using spherical lenses for both L_{p1} and L_{p2} , as described in section 5.1. Figure 6.2 plots the resulted longest wavelengths against dissipated power. The average maintained heat sink temperature, plus-minus its standard deviation, is stated in each of the subplots. The straight lines correspond to the linear fit (3.5). The inset text in black takes note of this fit, displaying the fit parameters in values. The stated thermal resistance results from the ratio of the two fit parameters (3.2)

$$R_{\text{th}} = \frac{\partial T}{\partial D} = \frac{\partial \lambda}{\partial D} / \frac{\partial \lambda}{\partial T}.$$

In order to obtain the fit we consider only the data points corresponding to the linear light-light conversion regime – the same as for estimating the conversion efficiency in section 6.1.1, Fig. 6.1. This means we exclude both, threshold and roll over segments.

Figure 6.3 shows the scaling of R_{th} with respect to spot size. The plot to the left displays the behavior noted in [17] and highlighted in section 3.4: the thermal resistance

decreases less efficiently than by area. The reduction in R_{th} is closer to w^{-1} than w^{-2} , as illustrated by the slope given in the log-log plot.

A VECSEL device is thin compared to the pumped area. The expected heat flow is one dimensional, independent on lateral cooling. The observed scaling behavior shows this approximation is not tenable. In an attempt to understand this behavior when we look at the expected temperature profile from Fig. 4.2. The temperature peaks at the center in the case of the depicted Gauss and super-Gaussians and, consequentially, lateral heat transfer occurs, beside the one-dimensional extraction [28].

The measurements conducted with the achromatic lens could not be used to extract the thermal resistance with the method described in section 3.1. Fit (3.5) relies on a linear relation between λ and D [16]. As will be discussed in section 6.3, Fig. 6.8, this linearity was not given.

The fit in turquoise corresponds to (3.9). With only three data points available to fit three parameters we cannot judge how good the found parameters actually are. But given the original meaning of a_3 – an outer radius of a VCSEL – we recognize the found values not to make too much sense. The found fit is valid only for spot sizes smaller than $2w = 550 \mu\text{m}$. This, together with the large uncertainties attached to the estimates of the thermal resistance, show there needs more work to be done in order to get a useful statement out of the analysis of R_{th} .

6.2 Optimized emission output

Given the insights from section 6.1 we try to optimize the emitted output further. The following two optimization strategies for the VECSEL output power are proposed based on a microscopic many-body physics simulation [11]. The first is to AR coat the sample: with a $3/4\lambda$ coating appropriate for the pump wavelength the reflection from the air–VECSEL cap interface (in our case InP) should reduce without changing the conditions for the emission wavelength. This intervention permits more of the incident pump to enter the structure, which increases the over all wallplug efficiency. The second optimization is to use a reflecting metalization layer behind the DBR – while leaving the DBR transparent for the pump. This results in the pump light passing the active region once more.

We investigate these two strategies in the lens configuration with the achromatic lens and a $333 \mu\text{m}$ pump spot diameter. First, we want to record the characteristics of sample 1 in more detail. Once we know these, we can apply the AR coating on this sample in order to compare with its uncoated state directly. For the second strategy we have to use a different sample; sample 2. Its specifications for the active region and DBR are identical with the ones from sample 1. The difference is a different treatment of the gold layer contacting the diamond heat sink: by reducing the amount of Ti used to adhere the DBR to the gold, this layer shows an increase in reflectivity.

The light-light characteristics resulting from this more detailed analysis is shown in Fig. 6.4. Each data point is measured $N = 5$ times, as opposed to only $N = 3$ for section 6.1. The irradiated spot is labeled B in Fig. 5.4. For this spot the sample performed best. On the other hand, our setup is not designed to scan the surface in a structured manner. The found maximum could be only a local maximum.

6.2.1 AR coating

The first optimization strategy [11] is to apply an anti-reflectance (AR) coating on the sample. In order to have a direct comparison we decided to coat sample 1. However, after this treatment, the surface roughness had visibly worsened. In particular, during aligning the output coupler, in a first step we overlap the pump spot with its reflection from the output coupler, using the visible aid of a camera along the emission path, see

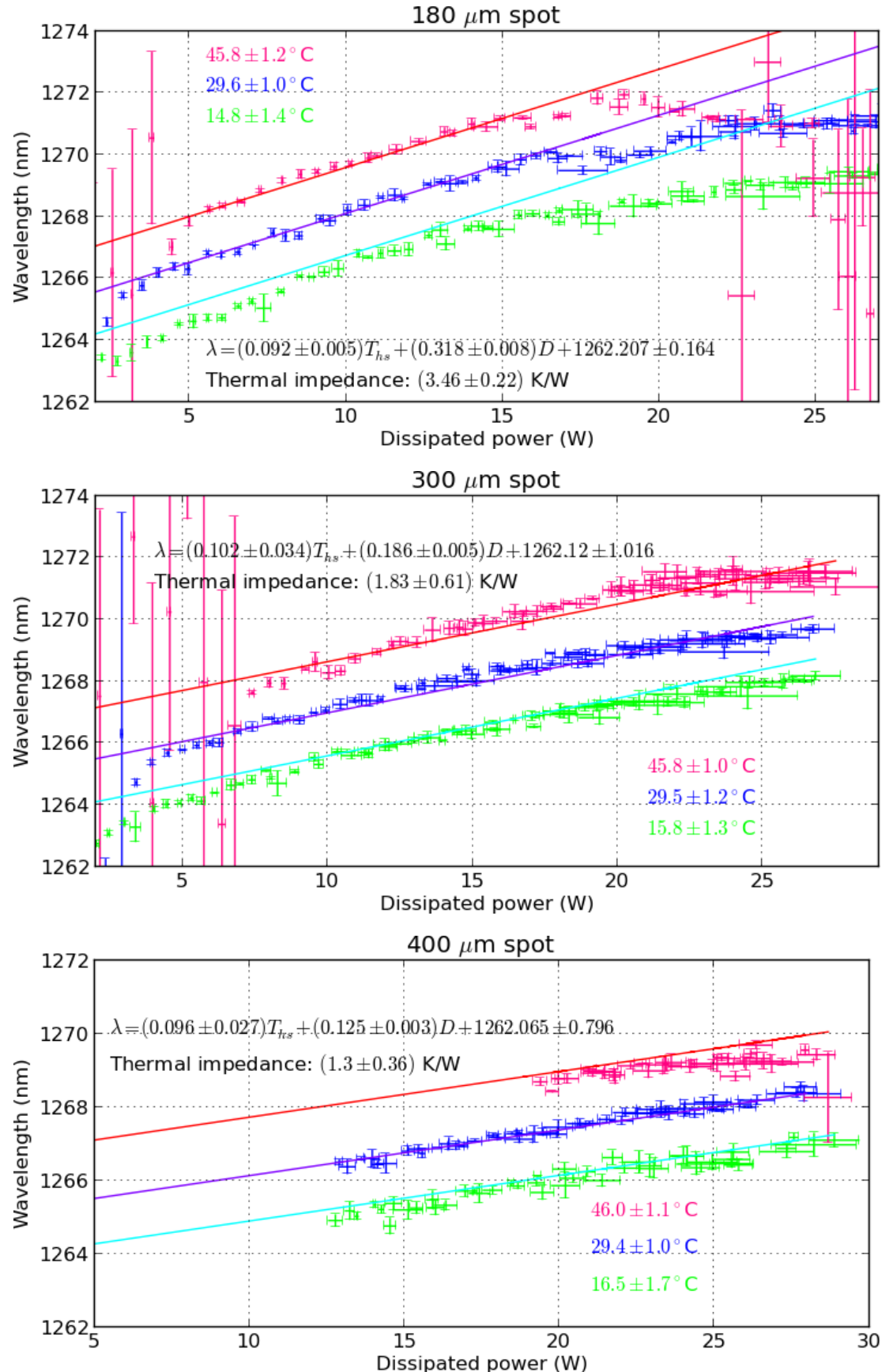


Figure 6.2: Estimating R_{th} with the method described in section 3.1 for three pump spot sizes. The straight lines correspond to the fit (3.5), taking into account only the part of linear light-light conversion – i.e. without the threshold or roll over segments.

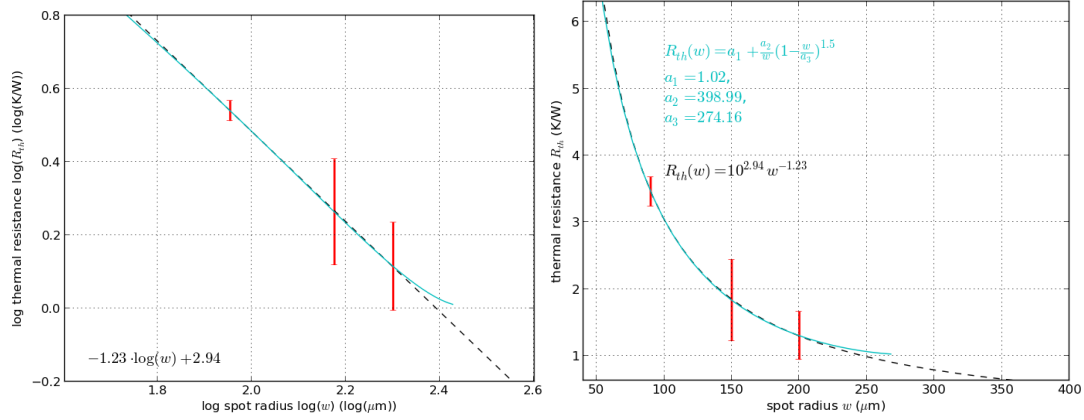


Figure 6.3: Scaling of thermal resistance (from Fig. 6.2) with spot size. Its dependency on spot diameter is expected to be closer to $(2w)^{-1}$ than $(2w)^{-2}$; i.e. not to scale with area [17]. This is visualized by the slope in the log-log plot (left). The continuous curve in turquoise shows a fit to an empirical curve (3.9) [17, 22]. Right, what the fits look like with linear axes.

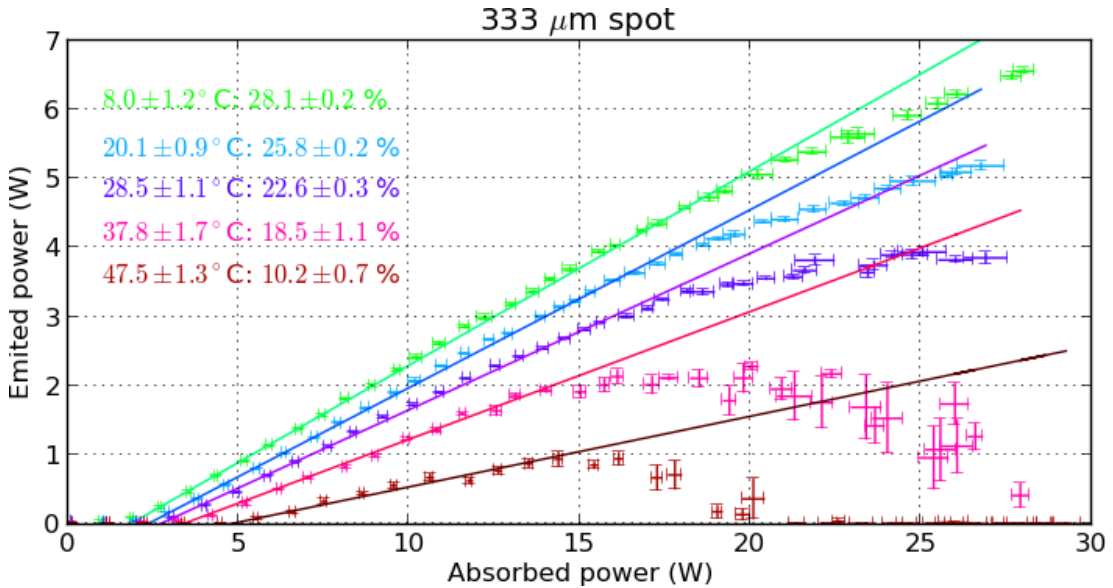


Figure 6.4: Detailed LL of sample 1. Irradiating spot B denoted in Fig. 5.4. Each data point is measured $N = 5$ times. The error bars correspond to the standard error.

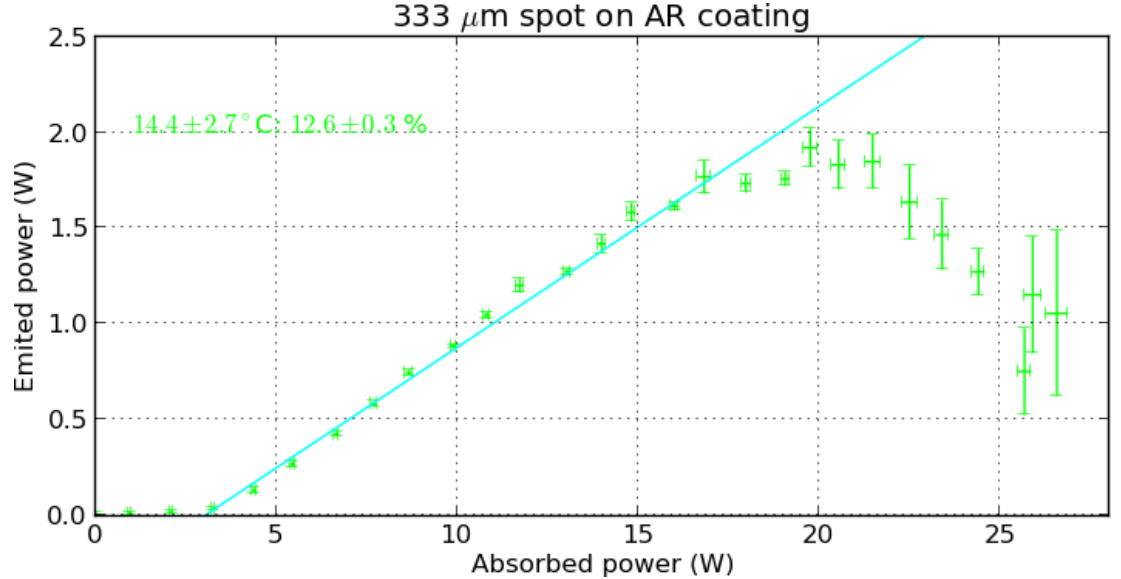


Figure 6.5: The AR coating applied on sample 1 worsened its performance. Given the observations made during measurements (see text), this is a verdict most likely not tenable for AR coating in general, but concerns the quality of our coating in particular.

appendix A. Once we have found a lasing configuration we rely on the power meter to find the optimum alignment.

In the case of the AR coated sample the second spot was hardly visible, and looked patterned; similar to a plastered wall. Unsurprisingly, the resulting light-light performance is clearly weaker than without the coating. Figure 6.5 shows the resulted light-light conversion.

Based on the stated observations, we cannot compare the two measurements. We have to improve the coating process before we can evaluate this optimization strategy.

6.2.2 Reflecting metalization layer: record output

For the second optimization strategy [11] we use a sample whose metalization interface between DBR and CVD diamond was treated to be highly reflective. Sample 2 is measured irradiating the spot indicated with a red circle in Fig. 5.6. The light-light characteristic is depicted in Fig. 6.6.

Apparently, a lot more of the absorbed light is converted into laser output (nearly 60 % at 5 °C heat sink temperature). On the other hand, the over all reflectivity off the sample is higher for sample 2 than for sample 1. This fact I revisit in section 6.4.

Table 6.1 highlights the observed peak performances. These, coincidentally, represent the new (unofficial) world record in emitted power in the 1300 nm waveband. The highest reported emission power for this waveband so far was 7.1 W in a intracavity heat spreader configuration using a pump spot diameter of 300 μm at a heat sink temperature of 7 °C [6].

Figure 6.7 shows a comparison between sample 1 (uncoated) and sample 2. The latter appears to be about twice as efficient in converting the absorbed light. However, this cannot directly be attributed to the second pass through the active region with this optimized design. In sample 1 we don't distinguish whether the pump is absorbed in the active or the metalization layer. Our definition of absorbed power, $A = P - R$ (5.1), looks only at the difference of power in the pump and the reflection channel. The contribution from the reflected power is indeed larger for sample 2, discussed in section 6.4.

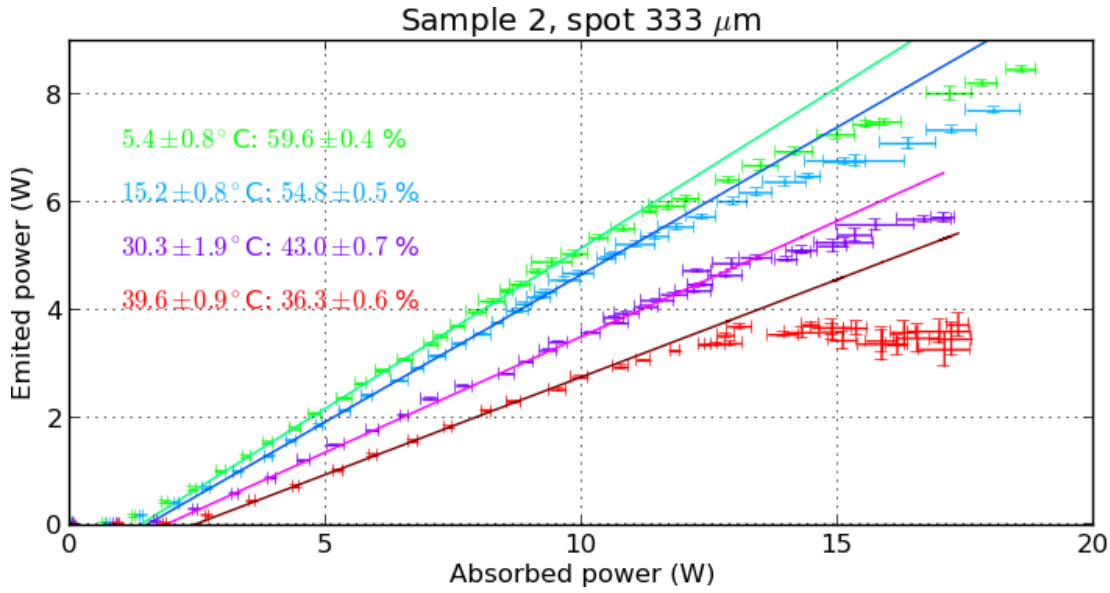


Figure 6.6: Light light performance of sample 2, with the gold interface between DBR and CVD diamond treated to be highly reflective. The irradiated spot is indicated in Fig. 5.6. Each data point represents an average over 5 repetitions.

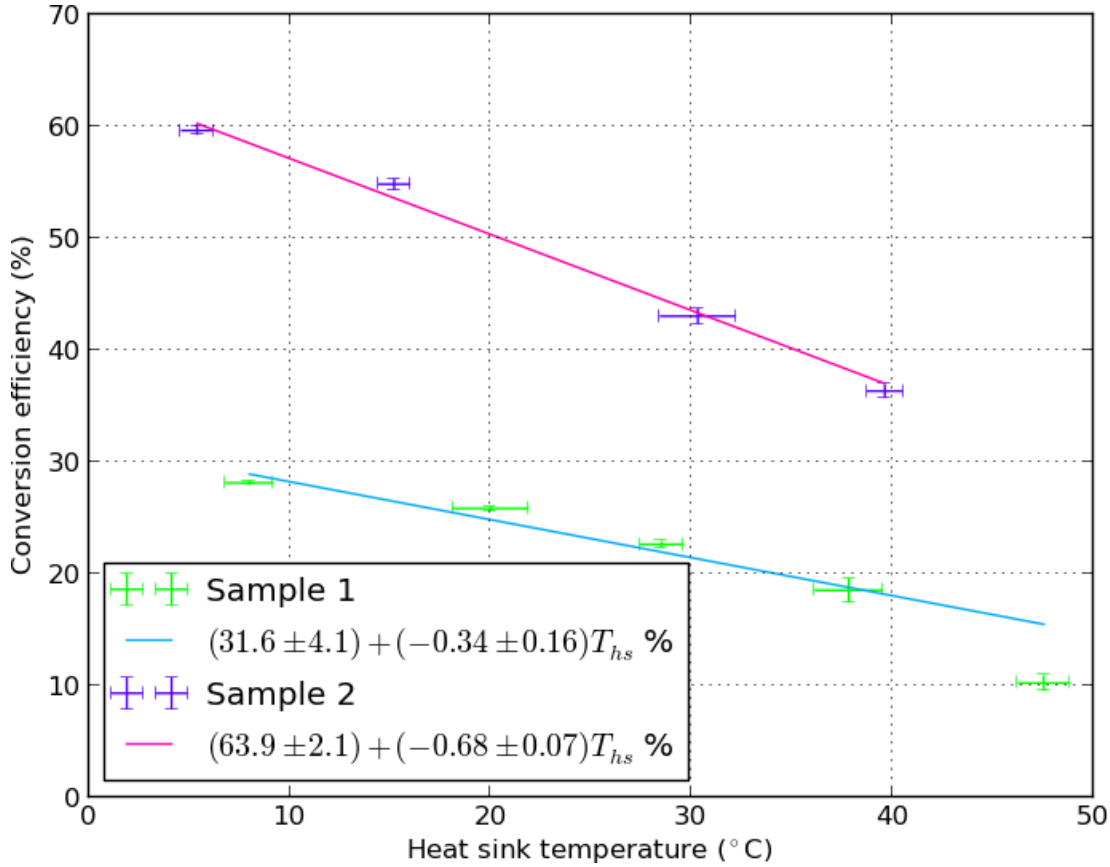


Figure 6.7: Summary of the values found in Fig. 6.4 and 6.6. The conversion efficiency of sample 2 corresponds to approximately twice the value of sample 1. The ultimate limit of conversion efficiency is given by the quantum defect $\lambda_{\text{pump}}/\lambda_{\text{laser}} = 77.5\%$.

Table 6.1: Highlighting the peak data from Fig. 6.6. The error values correspond: to the standard deviation for the heat sink, and to the standard error (5.3) for the absorbed and emitted power. Pump spot diameter is estimated as $333\ \mu\text{m}$. The incidence angle is $\approx 36^\circ$.

| Heat sink ($^\circ\text{C}$) | absorbed power (W) | emitted power (W) |
|--------------------------------|--------------------|-------------------|
| 5.4 ± 0.8 | 18.6 ± 0.3 | 8.46 ± 0.06 |
| 15.2 ± 0.8 | 18.1 ± 0.5 | 7.7 ± 0.06 |
| 30.3 ± 1.9 | 17.1 ± 0.2 | 5.72 ± 0.09 |
| 39.6 ± 0.9 | 17.4 ± 0.2 | 3.7 ± 0.2 |

6.3 Intrinsic roll over temperature

One method to estimate the thermal resistance looks at the dissipated power at roll over, linked with the heat sink temperature – see section 3.2. This method relies on an intrinsic roll over temperature, independent of the heat sink temperature: we associate the longest emitted wavelength with a temperature in the active region. If roll over occurs because the active exceeds a critical temperature, the emitted wavelength at this point should be the same regardless of the heat sink temperature

$$T_{\text{ro}} = T_{\text{hs}} + R_{\text{th}} D_{\text{ro}}. \quad (6.1)$$

We don't know whether all VECSEL structures show this behavior, or whether it depends on the device. It is thus necessary to first test the hypothesis by looking at the spectrum emitted at roll over. Once this is established the method described in section 3.2 is more convenient for estimating R_{th} .

Our measurements were pump limited. Not every investigated spot size and heat sink temperature did reach roll over. This would be necessary in order to extract the thermal resistance with said method. However, I can highlight the emitted spectra of those settings that did reach roll over.

The pump spot size scaling measurements of sample 1 depicted in Fig. 6.2 suggest an ultimately longest emitted wavelength of about 1271 nm. In the case of the $180\ \mu\text{m}$ the measurements corresponding to a heat sink temperature of $30\ ^\circ\text{C}$ and $45\ ^\circ\text{C}$ both even out at this wavelength.

In the configuration with lens $L_{\text{p}1}$ being achromatic the observed spectrum behaves differently. Figure 6.8 shows this exemplary for the spectra corresponding to the measurements presented in Fig. 6.4. The longest emitted wavelength does not depend linearly on dissipated power.

Consequentially, I cannot apply the linear regression suggested in 3.1, [16], in order to extract R_{th} . In principle, I could evaluate the derivatives $\frac{\partial \lambda}{\partial D}$ and $\frac{\partial \lambda}{\partial T}$ numerically. However, due to the fluctuations on D it is not clear how to evaluate $\frac{\partial \lambda}{\partial T}$ in practice. I therefore withstand to call out a number for R_{th} based on the presented results.

Concerning longest emitted wavelength, in Fig. 6.8 we see the measurements corresponding to $T_{\text{hs}} = \{48, 38, 29\} \ ^\circ\text{C}$ to converge to the same value. This limit wavelength is, however, longer than suggested by Fig. 6.2. The spectrum of sample 2, plotted in Fig. 6.9, does not allow to infer on the behavior of the peak wavelength.

In conclusion, the available data on emitted longest wavelength do not give a clear picture whether λ_{ro} is independent of the heat sink temperature or not. On the other hand, even if the assumption of an intrinsic roll over temperature is valid, there is another problem with the method presented in 3.2: it is supposed to be less error-prone, as mode fluctuations between two measurements are expected to yield a considerably large uncertainty in λ [16]. As shown in section 6.1.2 the obtained values for R_{th} , using the spectra dependent method 3.1, indeed do have a large uncertainty attached. But this

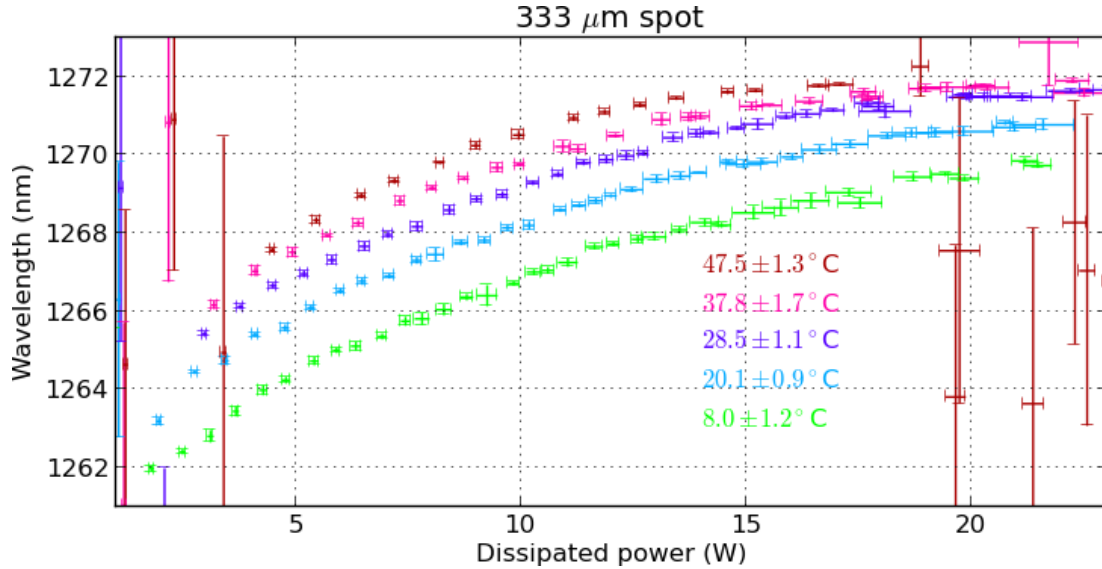


Figure 6.8: Longest emitted wavelength recorded in the achromatic lens configuration of sample 1. The observed non-linear relation was not expected given the discussion in section 3.1. The longest emitted wavelength over all seem to converge to a heat sink independent value. This is in line with the hypothesis of an intrinsic roll over temperature suggested in section 3.2.

comes not from the uncertainty of the single data points. The error bars along λ are small compared to the fluctuations in estimated dissipated power.

Ultimately, the uncertainties attached to the extracted thermal resistance come from the assumption $\frac{\partial \lambda}{\partial D}$ and $\frac{\partial \lambda}{\partial T}$ to be linear. Likewise, at least in our setup, the exact point of roll over is difficult to estimate. Therefore, deducing R_{th} using the roll over point does not result in a more accurate value.

6.4 Pump-induced change in reflectivity

We monitor the reflectivity of the sample during the measurements. The amount of reflected light is an important quantity to estimate the dissipated power D (3.6), which itself is important in order to asses the heat flow in the VECSEL device [16]. It turns out, the reflected fraction is not constant. Instead, it depends on the incident pump power and the heat sink temperature.

This observation of reflectivity was so far not reported in literature. In this section I present the general observations, followed by a more detailed analysis of the reflectivity in the low pump regime – what I will call base reflectivity. The section closes presenting some potential effects that may contribute to this phenomenon.

6.4.1 Observation

The reflectivity off the VECSEL structure, $r = R/P$, changes depending on the heat sink temperature and the pump power. Figure 6.10 illustrates this statement.

On the one hand side, the reflectivity decreases for an increase in heat sink temperature. With higher absorbed power the temperature inside the device increases further. However, for higher absorbed power the reflectivity increases. Consequentially, the pump induced change in reflectivity cannot be a purely thermal effect.

The lasing activity of the device potentially affects the reflectivity. In order to test for this, I measured the reflected light when we remove the output coupler. Figure 6.11 plots three temperatures measured with (depicted in Fig. 6.10) and without the output coupler.

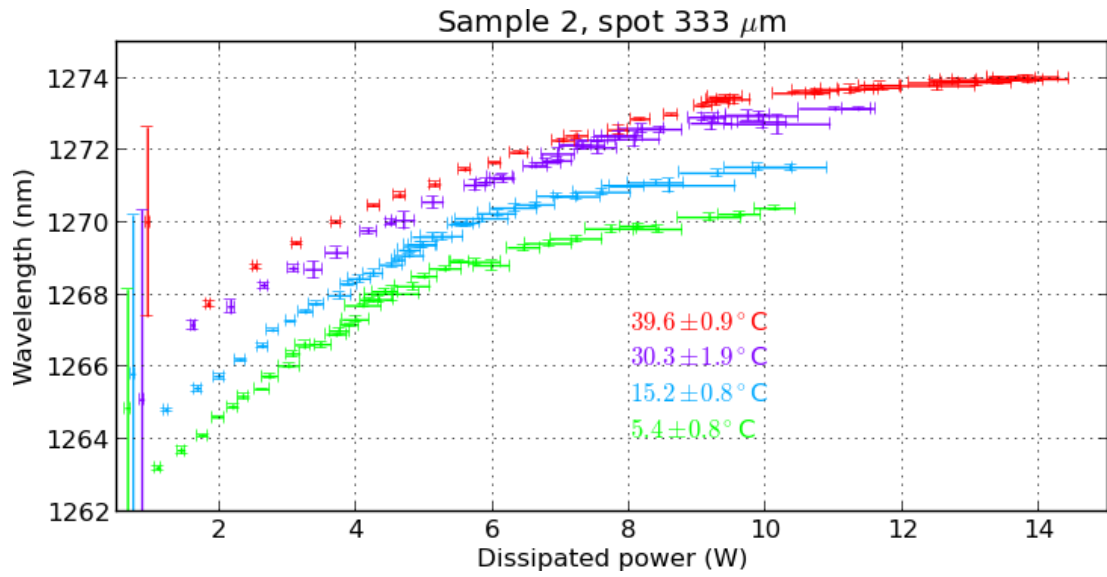


Figure 6.9: Longest emitted wavelength recorded in the achromatic lens configuration of sample 2. The over all longest emitted wavelengths appear not to converge to the same value for each of the heat sink temperatures.

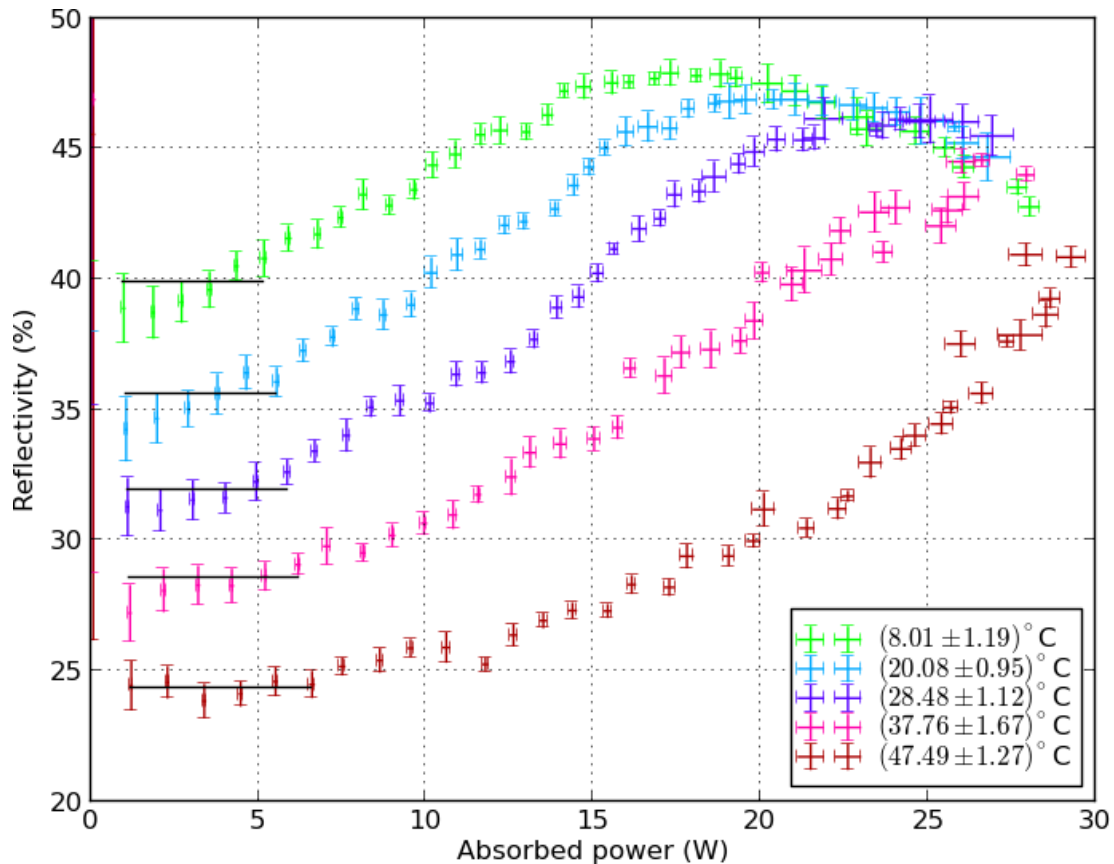


Figure 6.10: Sample 1. The reflectivity changes depending on pump power and heat sink temperature.

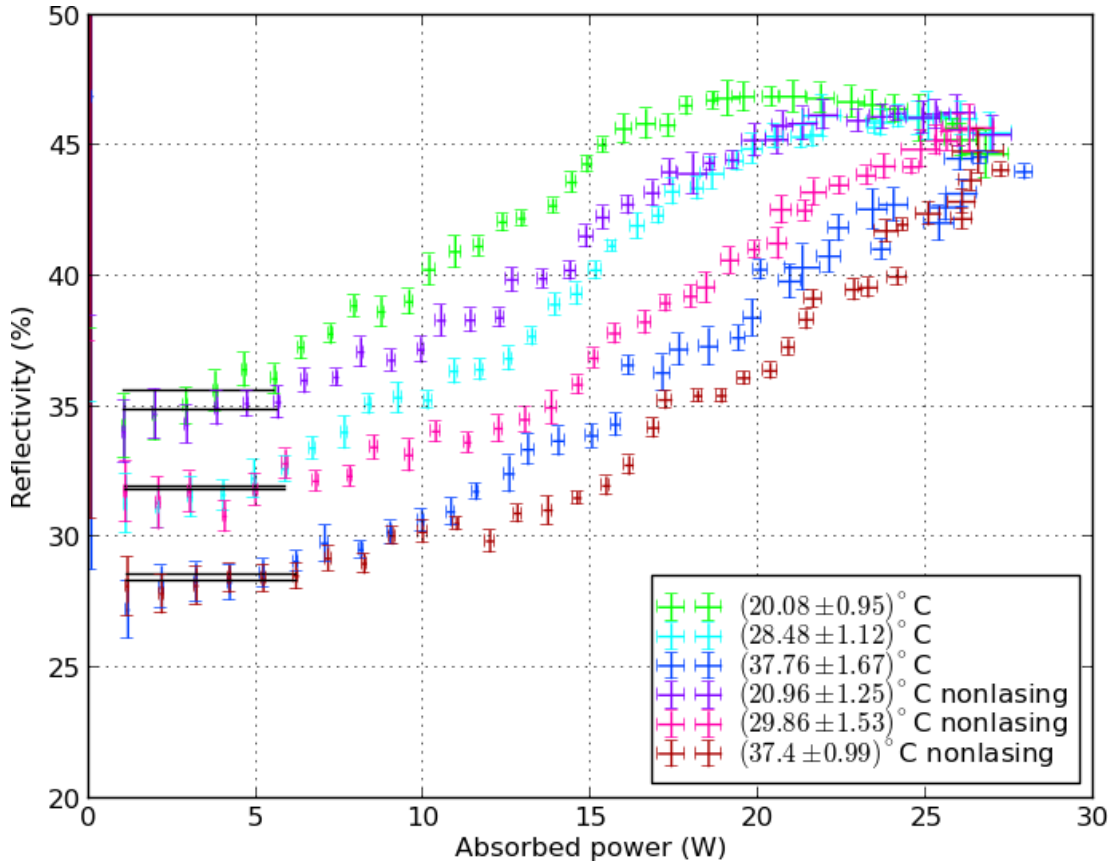


Figure 6.11: Sample 1. Reflectivity without output coupler.

The low pump regime reflectivity (base reflectivity) is unaffected by the presence or absence of the output coupler. Increased pump leads to an increase in reflectivity; qualitatively similar to the lasing configuration. But, quantitatively, this increase is less steep when we remove the output coupler.

Once the reflectivity has reached its peak value it decreases again. The point of peak reflectivity does not coincide with an apparent effect in the light light performance, Fig. 6.4.

We have treated sample 1 with an anti-reflectance coating, in an attempt to investigate an optimization strategy, laid out in section 6.2.1. Figure 6.12 demonstrates the base reflectivity indeed to be lowered. The AR coated device also shows an increase in reflectivity for higher pump.

In Fig. 6.10–6.14 the relative reflectivity, $r = R/P$, is plotted against absorbed power $A = P - R$. A priori it is not clear whether this is a good choice. However, by doing so the reflectivity curves of the different heat sink temperatures overlap in the decrease regime after the peak reflectivity. This overlap is present for both samples, and even more apparent in Fig. 6.14 of sample 2. Maybe, this hints at an intrinsic limit of the VECSEL structure. Plotting P for the x-axis, the declining line of the different heat sink temperatures are shifted with respect to each other. With D for the x-axis, the data points corresponding to the lasing configurations in Fig. 6.11 are shifted left, such that those without the output coupler overshoot the stated line of decreasing reflectivity.

6.4.2 Base reflectivity

For low pump power the relative reflectivity shows a flat plateau. The weighted mean reflectivity of the regime between 1–9 W of pumped power I call base reflectivity (the 9 W

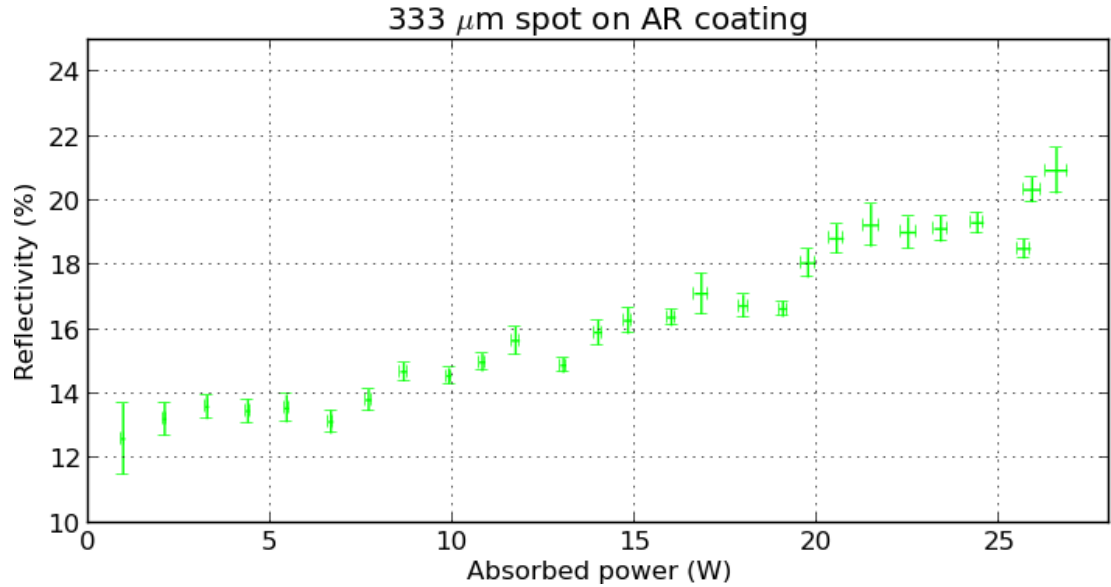


Figure 6.12: Sample 1 AR coated. While the AR coating wasn't successful to improve the light-light performance, the base reflectivity indeed was reduced. The heat sink temperature was $14.4 \pm 2.7^\circ\text{C}$. The uncoated sample showed a base reflectivity of about 38 % for this temperature. The coating hence successfully lowered the reflectivity to about a third.

is an arbitrary cut, based on Fig. 6.10). This base reflectivity follows a linear relation as a function of heat sink temperature. This is plotted in Fig. 6.13 and 6.14 for sample 1 and 2, respectively.

Sample 2 seems to be about 50 % more reflective than sample 1. Qualitatively, the increase in reflectance can be expected. By reducing the amount of Ti used to connect DBR with Au, the amount of reflected pump light from this interface increases [11]. This is exactly the difference between sample 1 and 2, see section 2.

6.4.3 Explanation candidates

The low pump regime should be governed by the simple reflectivity due to the multi layer nature of our device. In order to calculate this reflectivity value we need to know the refractive indices and absorption coefficients of all the used AlInGaAs compounds in our structure. We don't have access to such a complete table, so I cannot calculate this numeric limit.

Literature does not provide a satisfying answer for this pump induced reflectivity change. The effect of thermoreflectance appears to be a related candidate. It is used for temperature measurements based on the change in surface reflectivity [30, 31]. Accordingly, the incident pump perturbs the thermal equilibrium of the probed structure. The reflectivity then changes as a result of this induced modulation. In semiconductors, the relationship between the variation in optical reflectivity and temperature is mainly due to the temperature dependence of the band gap [32],

$$\Delta R = \frac{dR}{dT} \Delta T. \quad (6.2)$$

The thermoreflectance coefficient $\frac{dR}{dT}$ varies strongly with the probed material and the probe wavelength. It cannot reliably be simulated numerically, but has to be determined experimentally [31]. This procedure is time and equipment intensive. For this report I omit determining the thermoreflectance coefficient of the sample at hand. Consequentially, I cannot fit the expected thermoreflectance curve onto the measured behavior.

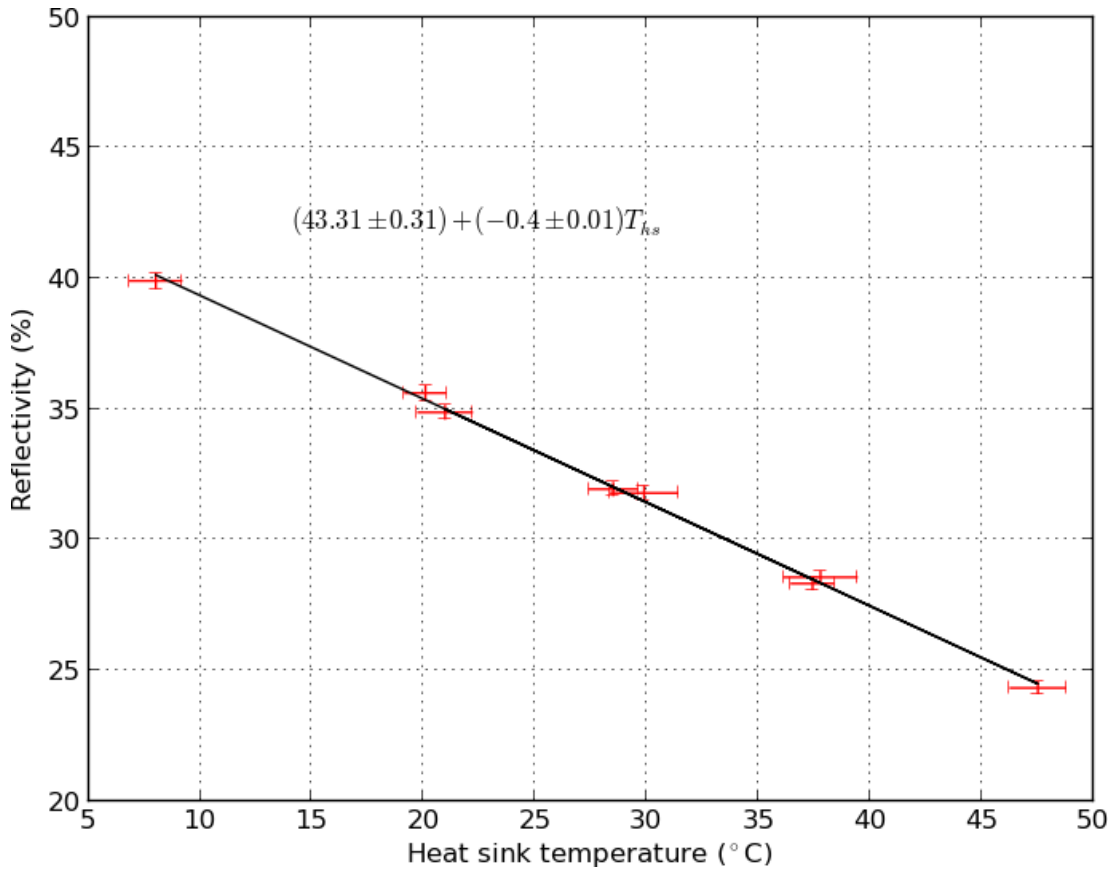


Figure 6.13: Sample 1. The base reflectivity follows a linear relation with the heat sink temperature. The presence of the output coupler does not affect this low pump regime. The corresponding measurements are therefore included. See Fig. 6.10 and 6.11.

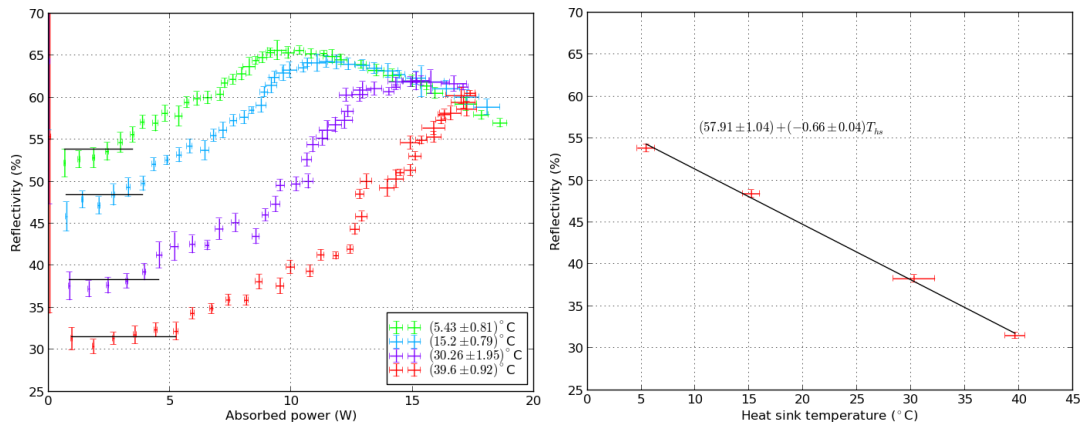


Figure 6.14: Sample 2. The reflectivity is higher than that for sample 1. In sample 2 the gold layer connecting the DBR with diamond is reflective while for sample 1, it absorbs the residual pump. Compared to Fig. 6.13 sample 2 is about 50 % more reflective than sample 1.

And I cannot conclude whether this concept leads into the right direction.

The thermal change in refractive index is unlikely to be a relevant contributor to the pump induced change in reflectivity: it depends only weakly on temperature, $\frac{1}{n_{\text{InP}}} \frac{dn_{\text{InP}}}{dT} = 2.7(3) \times 10^{-5} \text{ K}^{-1}$ [33]. This change is relevant for the shift in emission wavelength and hence section 3.1. But reflectivity changes in the order of $R = |\frac{n-1}{n+1}|^2$, where temperature induced change in n is unlikely to be relevant.

On the other hand, the barriers are designed to absorb the incident pump light. Consequentially, the temperature dependent band gap change is of large relevance.

Given the observation that the change in reflectivity is not solely a thermal effect, we have to assume there are (at least) two different mechanisms at work. Motivated by the thermoreflectance, first, we attribute the decrease in base reflectivity to the band gap of the semiconductor: As a result of the elevated temperature the quantum wells show a more metallic nature. Such a structure can absorb the incident pump with higher efficacy, which leaves less power in the reflection channel.

A second contributing effect is due to the creation of electron hole pairs. By increasing the pump power, the electron hole pair creation depletes. At this point more of the incident light is not absorbed and can be reflected from one of the many layers.

The AR coated sample showed a decrease in base reflectivity, while the uprise for higher pump power persisted. This indicates the base reflectivity to be a result of the many layer structure, while the reflectivity increase is due to an internal change.

If the laser emission is solely relevant as a cooling channel, the curves with and without output coupler should overlap, when plotted against dissipated power. However, with dissipated power, $D = A - E$, the data points from the output coupler configuration would shift left, which increases the difference between the two curves even more.

Instead, the explanation of electron hole pair depletion expects the reflectivity to increase faster in the scenario the electron hole pairs are created due to the stimulated interaction with the cavity. In absence of the output coupler these pairs are still created because of thermal excitation, but at a lower rate. This is what we can see in Fig. 6.11.

Whether my simplistic argument concerning the bandgap and electron hole excitation is tenable, I leave open for someone else to discuss. One objection for example is that we don't see an excitation saturation in the emission measurements. Secondly, this explanation is held very generally so that the observed effect should appear also in other VECSEL structures. I cannot find a publication describing our observations.

7 Conclusion

I have presented the power scaling behavior of our wafer-fused 1300 nm waveband VECSEL device in the thin disk (flip-chip) heat dissipation scheme. This scaling was found to be below the expected behavior for disk lasers, but are in line with other published findings. It is assumed to be a result of the sub-area scaling of the thermal resistance – whose scaling behavior was also demonstrated in this report.

Changing the pump configuration to incorporate an achromatic lens, resulted in significantly improved output performance. In this configuration I have investigated upon two optimization strategies: (i) anti-reflectance (AR) coating, (ii) improved reflectivity of the Au bonding layer between DBR and heat sink. This second strategy resulted in record output power of 8.5 W for a heat sink temperature of 5 °C. The AR approach we had to abandon due to insufficient coating quality. The found difference in output performance as a result of changed pump conditions suggests the pump beam profile to be more important than usually assumed. As such, a carefully prepared pump is likely to improve a VECSEL's performance, while keeping the chip design.

The longest emitted wavelength, resulting from the heating of the VECSEL device due to increased pump power, appears to tend to a value that is independent of the applied heat sink temperature. This finding suggests the power roll over of our device to occur at an intrinsic critical temperature; this property was thus far not confirmed for our structure. It allows to determine the thermal resistance in a way that doesn't rely on a spectral shift of the emitted light.

Furthermore, I have presented the reflectivity off our VECSEL structure to change for higher pump power. This behavior has so far not been reported. By taking into account these measured reflectivity values – instead of assuming the reflectivity to remain at its low pump reflectivity level – also the found conversion efficiency of our device showed record results; up to nearly 60 % for 5 °C heat sink temperature.

Beside these direct results, I have assessed two methods to experimentally determine the thermal resistance of a VECSEL, that can be measured simultaneously with regular light-light characteristics. I have to conclude these methods not to yield a good figure of merit. The identified dependencies inevitably link the resulting thermal resistance with the setup it was measured with. I have showed these shortcomings by means of experiment – the spectral behavior varied as a result of the pump conditions – and numerical considerations.

The presented maximum output power reached during this project is limited by pump power, heat sink temperature stability, and the lack of control over the pump conditions – most notably the pump distribution. In addition, the investigated samples show a high reflectivity, such that a considerable amount of pump is wasted. For future works I suggest to invest time and resources directed at these domains. The sample reflectivity could also be exploited by using a mirror arrangement that recycles the reflected power and redirects it onto the pumped spot.

This report acts as basis to reach out to other groups, who have already heavily invested in numerical approaches: if the improvements in output performance indeed can be partially attributed to the change in pump profile, more effort should be put into investigating this aspect for VECSEL applications. One of the key arguments of VECSELs is their capability to convert low-cost pump light into high quality laser emission. If this conversion can be improved by simple modifications in the pump channel, such findings may benefit a large variety of VECSEL applications. Additionally, it will be interesting to see the detailed reflectivity behavior of other devices.

As a last point, the presented measurements have demonstrated the high degree of sample integrity: our wafer-fused devices did not show any signs of degradation. And this despite the fact that the samples were heated up and cooled down over a broad range of temperatures; the samples were exposed to beyond roll over pump powers; the pump irradiation did not occur in a smooth ramp order but were randomly sampled instead. These findings demonstrate a high device quality, obtainable by wafer fusion.

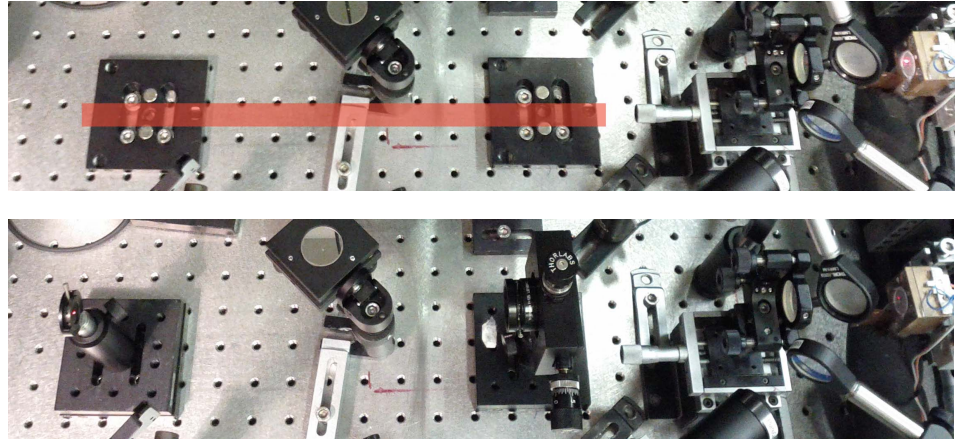


Figure A.1: Top: Removeable posts to define the beamline. Bottom: HeNe beam has to be directed through the two irises. With these two irises the position of the HeNe source is detached from the beam line.

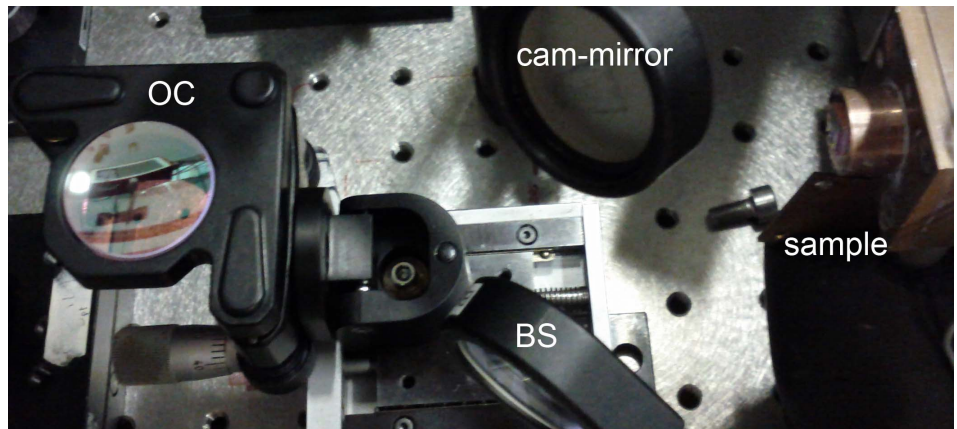


Figure A.2: First, we remove / flip all components along the beam line except the sample. In this configuration we align the sample surface orthogonal to the HeNe.

A Alignment process, description of

In order to align the different parts we employ a HeNe laser. Figure A.1 shows the beam line orthogonal to the sample surface. The beam line is defined by two removable magnetic posts. These posts allow us to remove and replace a mount reproducible. The beam line is ultimately defined by two irises. As such, we can place the HeNe source anywhere on the table; we simply have to guide its beam through these two irises.

For the alignment, in a first stage, we align the sample orthogonal to said beam line: We remove – or flip, Fig. A.2 – all other components along the beam line and leave only the sample. We adjust the orientation of the sample such that the back-reflection is directed at the HeNe, Fig. A.3. Once the sample is aligned we place the output coupler back in the beam path and repeat the same procedure.

In a last step we have to irradiate the sample with the 980 nm pump. A camera along the emission beam line sees the photoluminescence resulting from the pump on the sample. This camera is equipped with a long-pass filter in order to see only the photoluminescence and not the pump light. With this camera, initially, we see two spots corresponding to pump and reflection from the output coupler. Because of the aforementioned alignment with the HeNe laser these two spots should already be close, see Fig. A.4. We bring these two spots to overlap, using the xyz-stage of the output

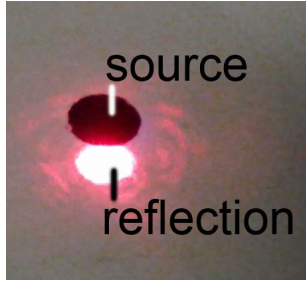


Figure A.3: By arranging the reflected beam to coincide with the HeNe source position we ensure the orthogonality of the component.

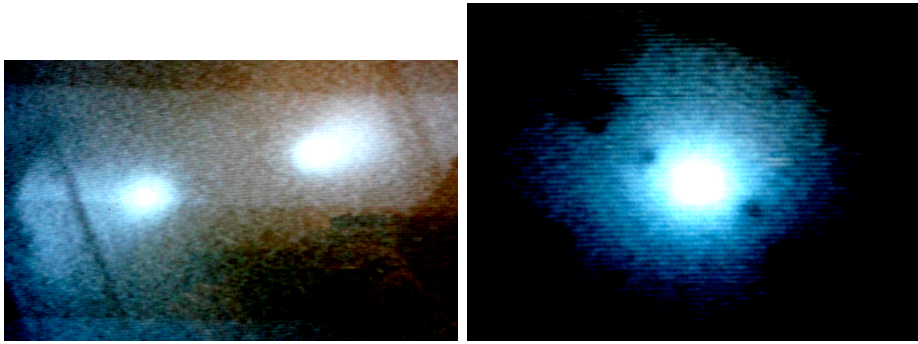


Figure A.4: After the pre-alignment with the HeNe, the two spots – originating from the pump and the output coupler reflection – are close by (left). By optimizing the alignment of the output coupler, these two spots have to be brought to overlap (right). Given this configuration, we have to increase the pump power, and at threshold we obtain laser emission. For the fine-alignment we have to replace the camera with a power meter and adjust for maximum output power.

coupler. Once the two spots do overlap, and the pump is above threshold, the sample starts lasing.

Figure A.5 shows an overview of the different components. The pump light is directed via fiber to a lens system that images the light onto the sample. With beam sampler BS_p we extract a fraction of the pump and direct it to detector det_p . This way we have a realtime reading of the pumped power. A considerable part of the pump light is reflected off the sample. This light diverges. First, we thus have to collimate it. For this we install a lens with appropriate focal length and distance from the sample. Of this reflected beam we again sample a fraction with BS_r , and direct this to detector det_r . The largest fraction of the reflected beam is directed to the beam dump. By sampling pump and reflection in this geometry we avoid high power readings on the detectors.

B Spatial filtering

In the focal plane of a lens, the intensity of the beam profile corresponds to its Fourier transform. To be more precise, in the Fraunhofer approximation (which is valid in the focal plane) we find the intensity of each point on the focal plane to be the amplitude of its respective spacial Fourier component [34]. We can use this fact in order to manipulate the beam profile; to spatially filter it. This method is based on the fact that Gaussians go into Gaussians under Fourier transform.

The core principle is simple: We start with a (Gaussian) wave. A first lens images this wave onto the focal plane. In this plane we place a mask. This mask performs an operation on the Fourier components present in the plane. A second lens collimates the

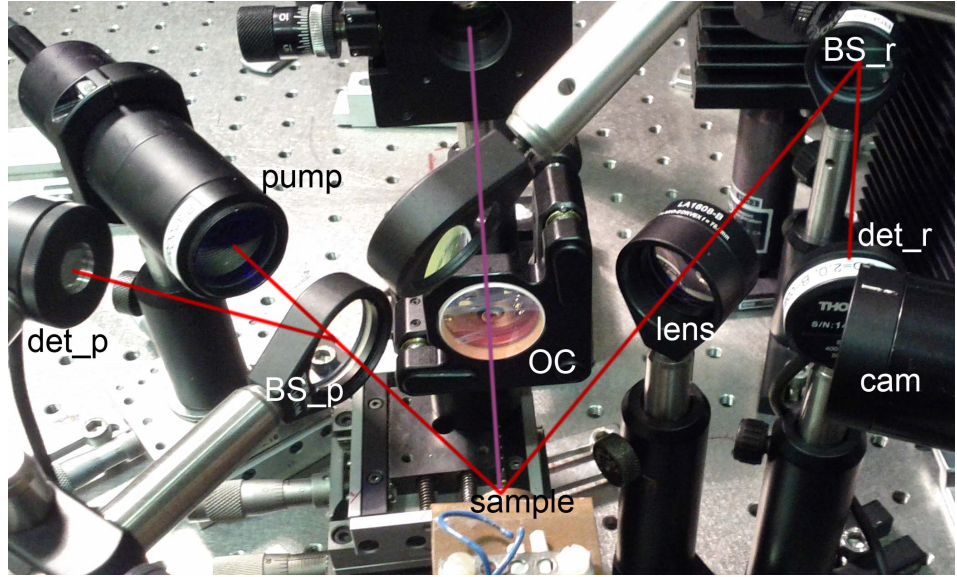


Figure A.5: Overview of the different components incorporated for the cavity.

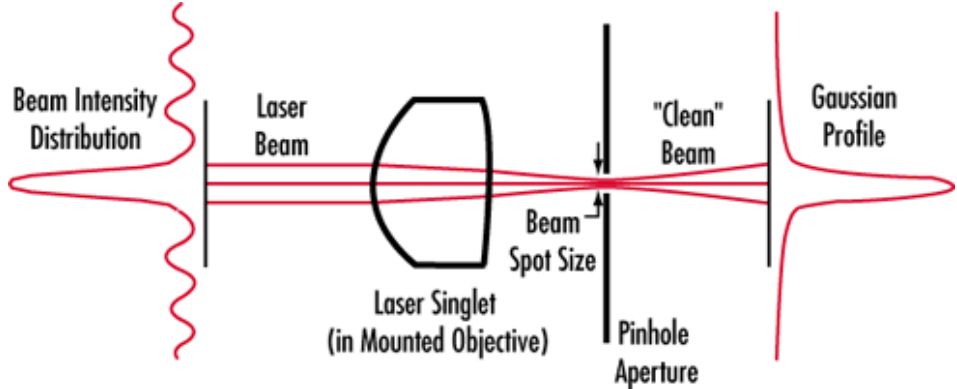


Figure B.1: Understanding Spatial Filters by Edmund optics [35].

now modified beam back.

One useful mask geometry is a pinhole – also known as low-pass filter. Noise and other impurities on the beam profile, picked up along the optical path, is represented by higher Fourier components. With a pinhole – with appropriate aperture diameter – we can cut off these higher components and keep only the basic Gaussian in the middle. Figure B.1 by Edmund optics illustrates this filtering.

As already said, the intensity in a point of the focal plane is given by the amplitude of its Fourier component ν_r . It is [34]

$$I = |\hat{g}(\nu_r)|^2, \quad (\text{B.1})$$

with \hat{g} the Fourier transform of a Gaussian beam

$$g(r) = \sqrt{I_0} \exp\left(-\frac{r^2}{w_0^2}\right), \quad (\text{B.2})$$

$$\hat{g}(\nu_r) = \int r dr d\varphi g(r) e^{i2\pi\nu_r r} \quad (\text{B.3})$$

$$= \sqrt{I_0} \pi w_0^2 \exp(-(\pi w_0 \nu_r)^2). \quad (\text{B.4})$$

In the focal plane the Fourier component is given as

$$\nu_r = \frac{r}{\lambda f}, \quad (\text{B.5})$$

with λ the wavelength and f the focal length of the lens. This results in an intensity distribution

$$I(r) = I_0(\pi w_0^2)^2 \exp\left(-2\left(\frac{\pi w_0 r}{\lambda f}\right)^2\right). \quad (\text{B.6})$$

The fraction of power contained within diameter D is hence [36]

$$\frac{P(r \leq \frac{D}{2})}{P_{\text{total}}} = \frac{2\pi}{P_{\text{total}}} \int_0^{D/2} I(r) r dr \quad (\text{B.7})$$

$$= 1 - \exp\left(-\frac{1}{2}\left(\frac{\pi w_0 D}{\lambda f}\right)^2\right). \quad (\text{B.8})$$

A diameter of

$$D = \frac{f\lambda}{w_0} \quad (\text{B.9})$$

permits 99.3 % of the total beam. Newport [36] recommends to use a pinhole with this diameter. Thorlabs on the other hand [37] suggests to employ a pinhole whose diameter is approximately 30 % larger. The transmitted power in this case would be 99.98 % of the total power.

By applying this method to the output of a multi mode fiber, we lose a considerable amount of this light; the Gaussian part corresponds to $\text{TEM}_{0,0}$. Starting with a Gaussian profile, other methods can be used e.g. to shape the beam into a super-Gaussian [29], in order to potentially optimize the mode overlap.

C COMSOL implementation

The commercial software COMSOL allows us to perform thermal simulations with a finite-element approach. The heat equation to be solved reads as

$$0 = \nabla(k\nabla T) + Q. \quad (\text{C.1})$$

It is k the thermal conductivity of the material ($[k] = \text{m}^{-1}$), and Q the heat source ($[Q] = \text{W/m}^3$); originating from the pump beam. Before we can talk about the numerical insights found with COMSOL, we have to understand the necessary parameters and their influence on this model.

C.1 Heat source Q

In order to understand how to investigate the temperature distribution within a VECSEL structure, we have to understand what input to provide to COMSOL to solve the heat equation (C.1). Our optical pumping represents a heat source Q . In this subsection I present what this quantity looks like, and what influence the different parameters – most notably, the beam profile – have.

The pump beam is assumed to be incident antiparallel to the z -axis (here referred to as from the top). We assume further it is of Gaussian profile – section 4.1 explains how to incorporate different pump profiles. In this configuration the heat source associated with each layer j of the structure is given as [3]

$$Q_j = \frac{2P}{\pi w^2} \eta_j \alpha_j e^{\frac{-2r^2}{w^2}} e^{-\alpha_j(z_{0j}-z)} e^{-\sum_{i < j} \alpha_i t_i}. \quad (\text{C.2})$$

The layers are counted from the top down – the sum $\sum_{i < j}$ includes the layers on top and ignores those below the layer of interest (in that case j). The meaning of the single parameters are listed in Tab. C.1. Furthermore we recognize

$$P' = P e^{-\sum_{i < j} \alpha_i t_i} \quad (\text{C.3})$$

to represent the power still remaining after layer $1, 2, \dots, j$. And

$$A = P' \eta_j \quad (\text{C.4})$$

corresponds to the absorbed power in layer j ; which heats by factor α_j .

Table C.1: Meaning of parameters used in (C.2).

| Parameter | Explanation | Unit |
|------------|-------------------------------------|-----------------|
| P | pump power | W |
| w | pump beam $1/e^2$ radius | m |
| α_j | absorption coefficient of layer j | m^{-1} |
| r | radial coordinate | m |
| z | axial coordinate | m |
| z_{0j} | coordinate of top of layer j | m |
| t_j | thickness of layer j | m |
| η_j | heat loading fraction in layer j | - |

The Gaussian beam assumed in (C.2) has an E-field [34]

$$E(r, z) \propto \frac{w_0}{w(z)} \exp\left(-\frac{r^2}{w^2(z)}\right) \exp(-i\Phi). \quad (\text{C.5})$$

The intensity of such a beam is proportional to the square modulus

$$I(r, z) \propto |E(r, z)|^2, \quad (\text{C.6})$$

$$I(r, z) = I_0 \left(\frac{w_0}{w(z)} \right)^2 \exp\left(-\frac{2r^2}{w^2(z)}\right). \quad (\text{C.7})$$

This is where the factor 2 in the exponent of (C.2) comes from. The over all power contained within the cross section is constant, P . Hence follows the last part of (C.2)

$$P = \int_0^{2\pi} d\varphi \int_0^\infty r dr I(r, z) \quad (\text{C.8})$$

$$= 2\pi I_0 \left(\frac{w_0}{w(z)} \right)^2 \int_0^\infty r dr \exp\left(-\frac{2r^2}{w^2(z)}\right) \quad (\text{C.9})$$

$$= 2\pi I_0 \left(\frac{w_0}{w(z)} \right)^2 \left[-\frac{w^2(z)}{4} \exp\left(-\frac{2r^2}{w^2(z)}\right) \right]_0^\infty \quad (\text{C.10})$$

$$= \frac{\pi}{2} w_0^2 I_0, \quad (\text{C.11})$$

$$\Rightarrow I_0 = \frac{2P}{\pi w_0^2}. \quad (\text{C.12})$$

C.2 Implementation of our VECSEL structure

In this subsection I discuss the parameters relevant for the actual COMSOL implementation, taking our structure as an example [2]. A schematic of our VECSEL structure is depicted in Fig. 2.2. Its fabrication details can be found in [2, 10]. A summary of the used parameters – in order to reproduce the presented results – is given in appendix C.4, Tab. C.2.

For the thermal conductivity we have to consider its spatial anisotropy. The radial and axial thermal conductivity we find with [14, 19, 38]

$$k_r = \frac{\sum_i k_i t_i}{\sum_i t_i} \quad (\text{C.13})$$

$$k_z = \frac{\sum_i t_i}{\sum_i k_i}, \quad (\text{C.14})$$

with the actual values calculated from [39]

$$k_{\text{Al}_x\text{Ga}_{1-x}\text{As}} = 0.55 - 2.12x + 2.48x^2 \text{ Wcm}^{-1}\text{K}^{-1}. \quad (\text{C.15})$$

Before we employ the extracted values of a bulk $\text{Al}_x\text{Ga}_{1-x}\text{As}$ material, we divide them in half. This way we account for the empirically observed decrease in thermal conductivity in a layered structure such as a DBR [40, 41].

The absorption coefficient α_g is chosen such that it matches with the measured single pass absorption of 50 % [2]:

$$e^{-\alpha_g t_g} = 0.5.$$

As a last important note we have to account for the reflected beam: it is absorbed in the gain section once again. Hence we implement a second heat source in this gain layer according to (4.2)

$$Q_{g_{\text{refl}}} = \frac{2P}{\pi w^2} \eta_{g_{\text{refl}}} \alpha_g e^{\frac{-2r^2}{w^2}} e^{-\alpha_g(z_{0g}-t_g+z)} e^{-\alpha_{\text{InP}}t_c - \alpha_g t_g - 2\alpha_{\text{InP}}t_{\text{sp}} - 2\alpha_d t_d}. \quad (\text{C.16})$$

In this we have the expression

$$\eta_{g_{\text{refl}}} = \eta_g(1 - \eta_{\text{au}}), \quad (\text{C.17})$$

that assumes the fraction of reflected light to be the residual light of what was not absorbed by the gold layer. This remaining part heats the layer with efficiency η_g . Furthermore we see the sign in the exponent

$$e^{-\alpha_g(z_{0g}-t_g+z)}$$

to be positive. This comes from the fact that in reflection the beam travels in the opposite direction.

C.3 Numeric convergence based on dimensionality

Measuring the performance of a sample in an experiment is not the same as simulating it numerically. With COMSOL we can exploit certain symmetries imposed by the structure. One is the radial symmetry around an irradiated spot, so that COMSOL has to solve the equations only in two rather than three dimensions – which speeds up the calculations. A second common simplification is to simulate the VECSEL dimensions only up to twice the size of the pump spot [3]. In order to ensure such simplifications don't lead to wrong conclusions, we have to investigate on the convergence behavior depending on these parameters. The names of parameters are taken from appendix C.1–C.2 and Tab. C.2.

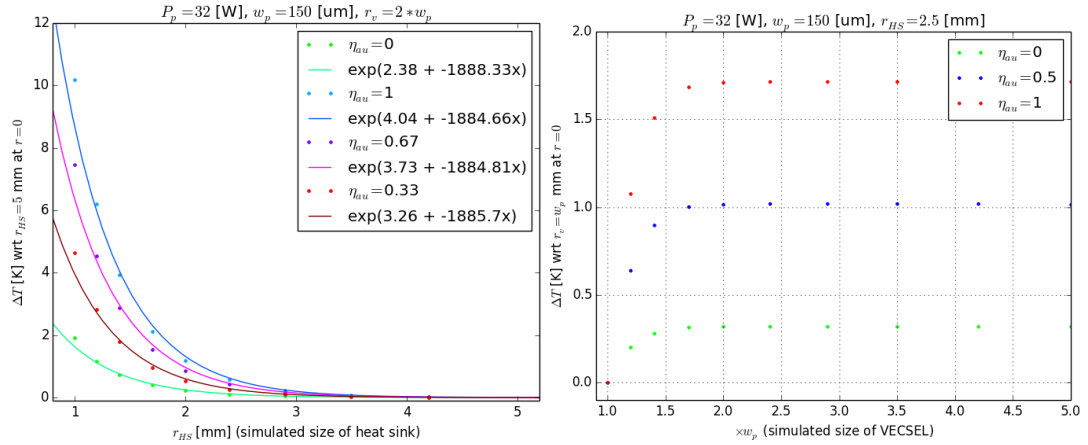


Figure C.1: Left: Investigating on the convergence of the result, depending on the system's dimension. The size considered for the heat sink is exponentially important. Right: Investigating on the convergence of the result, depending on the dimension of the VECSEL. Considering a system larger than $2w_p$ doesn't influence the over all result.

Figure C.1 (left) presents the convergence of the numerical result depending on the system's size. Each data point represents the following: I simulate the temperature on the surface of the structure caused by a $P = 32 \text{ W}$, $2w_p = 300 \mu\text{m}$ pump diameter beam. The radius of the VECSEL is held constant at $r_v = 2w_p$. In the center (at $r = 0$) the temperature is the highest; this is the value we store, for each system size r_{HS} ; the considered radius of the heat sink. For different values of η_{au} I look at various radii between $r_{HS} = 1 \text{ mm}$ and $r_{HS} = 5 \text{ mm}$ (twice the size of our actual structure with a cross section of $5 \times 5 \text{ mm}^2$). In the plot ΔT refers to the difference between the temperature obtained with the r_{HS} specified along the x-axis and the temperature with $r_{HS} = 5 \text{ mm}$.

The larger r_{HS} is chosen, the less relevant is its actual value – the temperature spread due to the extra bulk material goes exponentially. Therefore, it seems to be important to simulate the heat sink (diamond layer and copper bulk) as its full size. The size of the VECSEL on the other hand seems to be far less important; its over all volume and thus its ability to store and transfer heat is small. VESCEL sizes larger than two times the beam radius result in the same temperature increase. This statement is visualized in Fig. C.1 (right). In this plot, the heat sink is kept at constant $r_{HS} = 2.5 \text{ mm}$ and r_v is varied as multiples of w_p .

The influence of the considered thickness of the gold layer depends on whether or not the incident beam is absorbed in this interface – i.e. whether the gold layer only conducts the heat, or is itself a heat source. Figure C.2 (left) illustrates this consideration.

In order to look at the influence of the heat sink copper block we assume $r_{HS} = 2.5 \text{ mm}$, $r_v = 2w_p$, $t_{au} = 100 \text{ nm}$. The bottom boundary of the copper block is held at constant temperature. A thicker copper heat sink hence means that the heat has to travel a longer distance. As shown in Fig. C.2 (right) this extra distance is relevant; especially if we consider the gold layer to act as a heat source.

C.4 Explicit listing of simulation parameters

Because numerical simulations are difficult to reproduce when the used parameters are unknown, the ones I used for section 4 are listed in Tab. C.2.

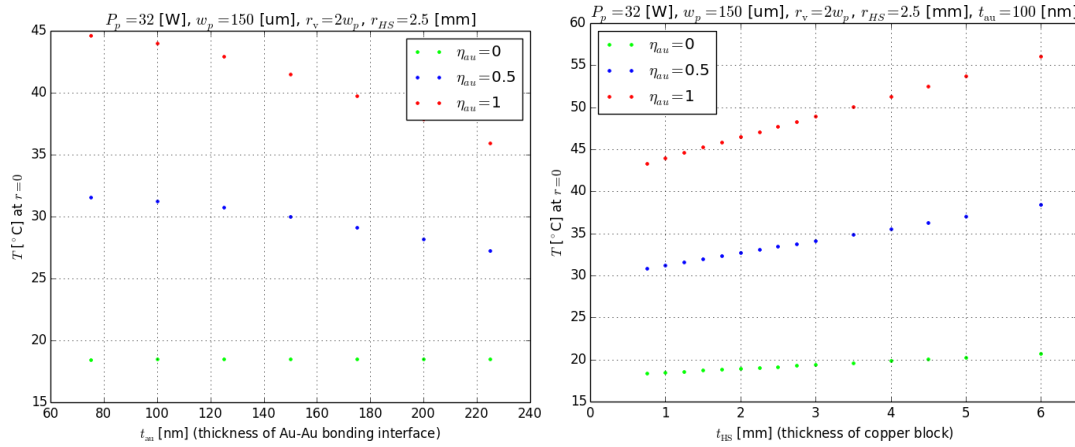


Figure C.2: Left: Investigating on the convergence of the result, depending on the thickness of the Au-Au bonding interface. If we assume the gold layer absorbs at least some of the incident beam, we have to know the thickness of this layer. Right: Investigating on the convergence of the result, depending on the thickness of the copper heat sink considered. Its importance depends on whether or not we assume the gold layer to act as a heat source.

References

- [1] A. C. Tropper, S. Hoogland, *Review, Extended cavity surface-emitting semiconductor lasers*, Progress in Quantum Electronics 30, 1–43, (2006)
- [2] A. Rantamäki et al., *High-power flip-chip semiconductor disk laser in the 1.3 μm wavelength band*, Optics Letters, Vol. 39, No. 16, (2014)
- [3] A. J. Kemp et al., *Thermal Management in 2.3-μm Semiconductor Disk Lasers: A Finite Element Analysis*, IEEE Journal of Quantum Electronics, Vol. 44, No. 2, (2008)
- [4] A. Chernikov et al., *Influence of the spatial pump distribution on the performance of high power vertical-external-cavity surface-emitting lasers*, Appl. Phys. Lett., vol. 97, no. 19, pp. 191110-1-191110-3, 2010
- [5] S. Calvez et al., *Semiconductor disk lasers for the generation of visible and ultraviolet radiation*, Laser & Photon. Rev. 3, No. 5, 407–434 (2009)
- [6] A. Sirbu et al., *High performance wafer-fused semiconductor disk lasers emitting in the 1300 nm waveband*, Optics Express, Vol. 22, Issue 24, pp. 29398-29403 (2014)
- [7] G. Baili et al., *Experimental demonstration of a tunable dual-frequency semiconductor laser free of relaxation oscillations*, Optics Letters, Vol. 34, No. 21, (2009)
- [8] M. Lukowski et al., *Widely Tunable High-Power Two-Color VECSELS for New Wavelength Generation*, IEEE Journal of Selected Topics in Quantum Electronics, Vol. 21, No. 1, (2015)
- [9] R. G. Bedford et al., *Power-limiting mechanisms in VECSELS* in Proc. Enabling Photon. Technol. Defense Security Aerospace Appl., (2005)
- [10] A. Sirbu et al., *Wafer-fused VECSELS emitting in the 1310 nm waveband*, Proc. SPIE 8966, 8966OG-1-8 (2014)

- [11] J. Hader et al., *VECSEL optimization using microscopic many-body physics*, IEEE J. Sel. Top. Quantum. Electron. 17, 1753 (2011)
- [12] A. J. Kemp et al., *Thermal Management in Vertical-External-Cavity Surface-Emitting Lasers: Finite-Element Analysis of a Heatspreader Approach*, IEEE Journal of Quantum Electronics, Vol. 41, No. 2, (2005)
- [13] B. Heinen et al., *106 W continuous-wave output power from vertical-external-cavity surface-emitting laser*, Electron. Lett. 48, 516 (2012)
- [14] S. L. Vetter, S. C. Calvez, *Thermal Management of Near-Infrared Semiconductor Disk Lasers With AlGaAs Mirrors and Lattice (Mis)Matched Active Regions*, IEEE Journal of Quantum Electronics, Vol. 48, No. 3, (2012)
- [15] M. Devautour et al., *Thermal Management for High-Power Single-Frequency Tunable Diode-Pumped VECSEL Emitting in the Near- and Mid-IR*, IEEE J. of Sel. Topics in Quant. El., Vol. 19, No. 4, (2013)
- [16] B. Heinen et al., *On the Measurement of the Thermal Resistance of Vertical-External-Cavity Surface-Emitting Lasers (VECSELs)*, IEEE J. Quantum Electron. 48, 934 (2012)
- [17] S. Giet et al., *Comparison of thermal management techniques for semiconductor disk lasers*, Proc. of SPIE Vol. 6871, 687115, (2008)
- [18] J. Hader et al., *On the measurement of the thermal impedance in vertical-external-cavity surface-emitting lasers* Journal of Applied Physics 113, 153102 (2013)
- [19] H. Lindberg et al., *Thermal Management of Optically Pumped Long-Wavelength InP-Based Semiconductor Disk Lasers*, IEEE Journal of Selected Topics in Quantum Electronics, Vol. 11, No. 5, (2005)
- [20] H. Q. Le et al., *Scalable high-power optically pumped GaAs laser* App. Phy. Lett. 58, pp. 1967–1969, (1991)
- [21] V.-M. Korpijärvi et al., *11 W single gain-chip dilute nitride disk laser emitting around 1180 nm*, Optics Express, Vol. 18, No. 25, (2010)
- [22] W. Nakwaski and M. Osinski, *Thermal resistance of top-surface-emitting vertical-cavity semiconductor lasers and monolithic two-dimensional arrays* Electronics Letters, 28(6), 72-574, (1992)
- [23] Thorlabs, *Achromatic Doublets*,
http://www.thorlabs.de/NewGroupPage9.cfm?ObjectGroup_ID=259
- [24] Thorlabs, *Power meter operation manual*,
<http://www.thorlabs.de/thorcat/19500/PM100USB-Manual.pdf>
- [25] R. J. Barlow, *Statistics – A guide to the use of statistical methods in the physical sciences*, The Manchester Physics Series, Wiley, (1999)
- [26] B. Efron, G. Gong, *A Leisurely Look at the Bootstrap, the Jackknife and Cross-Validation*, The American Statistician, Vol 37, No 1 (Feb 1983), pp. 36-48
- [27] C. Hessenius et al., *Lateral lasing and ASE reduction in VECSELs*, in Proc. Vertical External Cavity Surface Emitting Lasers, San Francisco, CA, 2011, pp. 791909-1-791909-8

- [28] A. Chernikov et al., *Heat management in high-power vertical-external-cavity surface-emitting lasers*, IEEE J. Sel. Topics Quantum Electron., vol. 17, no. 6, pp. 1772-1778, Nov.-Dec. 2011
- [29] J. D. Mansell et al., *Gaussian to Super-Gaussian Intensity Profile Conversion with Refractive Micro-Optics*, online <http://www.mansellassociates.com/CLEOTalk.pdf>, (2000)
- [30] P. W. Epperlein, *Micro-temperature measurements on semiconductor laser mirrors by reflectance modulation: a newly developed technique for laser characterization*, Jpn. J. Appl. Phys. 32, 5514-5522, (1993)
- [31] K. Pierscinski et al., *Investigation of thermal management in optically pumped, antimonide VECSELs*, Microelectron. J., vol. 40, no. 3, pp. 558-561, (2009)
- [32] G. Tessier et al., *Quantitative thermal imaging by synchronous thermoreflectance with optimized illumination wavelengths*, Appl. Phys. Lett. 78, 2267-071106, (2001)
- [33] Springer Materials, *The Landolt-Börnstein Database*, online <http://www.springermaterials.com>
- [34] U. Keller, *Lecture Quantum Electronics*, ETH Zurich, (2012)
- [35] Edmund optics, *Understanding Spatial Filters*, online <http://www.edmundoptics.de/technical-resources-center/lasers/understanding-spatial-filters>
- [36] Newport, *Spatial Filters*, online <http://www.newport.com/Spatial-Filters/144910/1033/content.aspx>
- [37] Thorlabs, *Principles of Spatial Filters*, http://www.thorlabs.de/NewGroupPage9.cfm?ObjectGroup_ID=997
- [38] M. Osinski et al., *Effective thermal conductivity analysis of $1.55 \mu\text{m}$ InGaAsP/InP vertical-cavity top-surface-emitting microlasers*, Electron. Lett., vol. 29, issue 11, (1993)
- [39] Electronic Archive, *New Semiconductor Materials, Characteristics and Properties*, online <http://www.ioffe.ru/SVA/NSM/>
- [40] J. Piprek et al., *Thermal Conductivity Reduction in GaAs-AlAs Distributed Bragg Reflectors*, IEEE Photonics Technology Letters, VOL. 10, NO. 1, (1998)
- [41] A. Rantamäki et al., *High power semiconductor disk laser with a semiconductor-dielectric-metal compound mirror*, Appl. Phys. Lett. 104, (2014)
- [42] J. Piprek et al., *What Limits the Maximum Output Power of Long-Wavelength Al-GaInAs/InP Laser Diodes?*, IEEE Journal of Quantum Electronics, VOL. 38, NO. 9, (2002)
- [43] E. F. Schubert, *Materials - Refractive index and extinction coefficient*, online <http://homepages.rpi.edu/~schubert/Educational-resources/Materials-Refractive-index-and-extinction-coefficient.pdf>, Rensselaer Polytechnic Institute, NY USA

Table C.2: Parameters used in the COMSOL simulation reported in section 4.

| | Quantity | Value |
|----------------|--|---|
| P_p | Pump power | 32 W |
| w_p | Pump beam radius ($1/e^2$) | $100 \mu\text{m}$ |
| t_c | Thickness cap [Specs] | $0.1017 \mu\text{m}$ |
| t_g | Thick. gain [Specs] | $0.7785 \mu\text{m}$ |
| t_{sp} | Thick. InP spacer [λ , Specs] | $0.4039 \mu\text{m}$ |
| t_d | Thick. DBR [Specs] | $5.0709 \mu\text{m}$ |
| t_{au} | Thick. Au layer [estimate] | 200 nm |
| t_{dia} | Thick. diamond layer | 0.3 mm |
| t_{HS} | Thick. copper heat sink | 3 mm |
| k_{InP} | Thermal conductivity InP [42] | $68 \text{ W}/(\text{K} \cdot \text{m})$ |
| k_g | Therm. cond. gain [42] | $4 \text{ W}/(\text{K} \cdot \text{m})$ |
| k_d | Therm. cond. DBR [40] | $0.35 \text{ W}/(\text{cm} \cdot \text{K})$ |
| k_{dr} | Therm. cond DBR in radial [14, 39, 40] | $36.8 \text{ W}/(\text{m} \cdot \text{K})$ |
| k_{dz} | Therm. cond DBR in z [14, 39, 40] | $34.6 \text{ W}/(\text{m} \cdot \text{K})$ |
| k_{dia} | Therm. cond. diamond [2] | $1800 \text{ W}/(\text{m} \cdot \text{K})$ |
| k_{au} | Therm. cond of gold [33] | $320 \text{ W}/(\text{m} \cdot \text{K})$ |
| α_{InP} | Absorption coeff InP at 980 nm [33, 39] | 0 mm^{-1} |
| α_g | Absorpt. gain [2] | $0.9 \times 10^6 \text{ m}^{-1}$ |
| α_d | Abs. DBR at 980 nm [33, 39] | 0 mm^{-1} |
| α_{au} | Abs. Au [33, 39, 43] | 86554 mm^{-1} |
| λ_p | Pump wavelength | 980 nm |
| λ_L | Laser wavelength | 1270 nm |
| η_c | Heat loading fraction: cap | 0 |
| η_g | Heat loading fraction: gain | $1 - \lambda_p/\lambda_L$ |
| η_{sp} | Heat loading fraction: spacer | 0 |
| η_d | Heat loading fraction: DBR | 0 |
| η_{au} | Heat loading fraction: Au | 0.75 |
| η_{grefl} | Heat load. frac.: Gain from reflected beam | $\eta_g * (1 - \eta_{au})$ |
| z_{0c} | Coordinate top of cap | $z_{0g} + t_c$ |
| z_{0g} | Coord top of gain | $z_{0sp} + t_g$ |
| z_{0sp} | Coord top of spacer | $z_{0d} + t_{sp}$ |
| z_{0d} | Coord top of DBR | $z_{0au} + t_d$ |
| z_{0au} | Coord top Au layer; Interf. Au-DBR to be at 0. | 0 m |
| z_{dia} | Coord bottom diamon layer | $z_{0au} - t_{au} - t_{dia}$ |
| z_{HS} | Coord bottom HS | $z_{dia} - t_{HS}$ |
| r_v | Width of VECSEL; small for better numeric | $2 * w_p$ |
| r_{HS} | Width of heat sink (and diamond) | 2.5 mm |
| T_C | 0 °C | 273.16 K |
| T_0 | Base temperature | $T_C + 15 \text{ K}$ |
| β | Exponent of Supergaussian | {3, 4} |
| a_β | normalization super-Gaussian | {0.5687, 0.6267} |